



DIPLOMARBEIT

Comparing Snow Melt Methods from Multi-Temporal Sentinel-1 SAR Backscatter Data

zur Erlangung des akademischen Grades

Diplom-Ingenieurin

im Rahmen des Studiums

Geodäsie und Geoinformation

eingereicht von

Melina Frießenbichler, BSc

01525794

an der Fakultät für Mathematik und Geoinformation
der Technischen Universität Wien

Betreuung

Univ.Prof. Dipl.-Ing. Dr.techn. Wolfgang Wagner

Univ.Ass. Davide Festa, PhD

Wien, am

22. Jänner 2024

Verfasserin

Betreuer



Die approbierte gedruckte Originalversion dieser Diplomarbeit ist an der TU Wien Bibliothek verfügbar
The approved original version of this thesis is available in print at TU Wien Bibliothek.

Affidavit

I hereby declare that this thesis has been composed entirely by myself and the work herein is my own. All exceptions are marked explicitly- including figures, tables and graphs - by referencing the source as borrowed. And I further confirm, that this thesis has not been submitted, in whole or in part, in any previous application and/or thesis.

Melina Frießenbichler, BSc, Wien, den 22.01.2024



Die approbierte gedruckte Originalversion dieser Diplomarbeit ist an der TU Wien Bibliothek verfügbar
The approved original version of this thesis is available in print at TU Wien Bibliothek.

Acknowledgements

First of all I would like to thank Claudio Navacchi and Davide Festa for giving me support throughout this thesis and lending an open ear for my questions. Of course I would also like to thank Prof. Wolfgang Wagner without whom it would not be possible to write this thesis at all. Further, I want to thank my fellow students for motivating me and together finding our first steps into the scientific community

My special thanks go to all my friends and colleagues for giving me the opportunity to investigate deeper into snow research, mostly in-situ, for both research purposes and personal adventures.



Die approbierte gedruckte Originalversion dieser Diplomarbeit ist an der TU Wien Bibliothek verfügbar
The approved original version of this thesis is available in print at TU Wien Bibliothek.

Abstract

The Global Climate Observing System (GCOS), cosponsored by the World Meteorological Organization (WMO) has categorized snow as one of the essential climate variables. This underlines the importance of snow-related research questions, especially at a time when the issue of climate change is omnipresent, both in the scientific community and in everyday life. Snowmelt research is essential as many people depend on snowmelt runoff from high alpine catchments. Little research has been done on snow melt events from remote sensing applications, mostly covering small areas and compared to in situ measurements. This thesis compares snow melt events from Sentinel-1 SAR backscatter data to river level fluctuations over a four-year period.

Two different approaches have been investigated to determine the day of snow melt over all catchments. The two approaches differ in their threshold settings and mathematical calculations. The first method classifies wet snow and identifies different states of the melting phase using a threshold, while the second method uses time series derivatives. After defining the catchments region for 35 water stations, 35 different catchment polygons are obtained. It is found that using the derivative method for calculating the runoff day did not work as good as by detecting the absolute minimum of the backscatters time series.

In addition, an elevation related threshold was introduced to discriminate the runoff date at different elevations. It was clearly noticeable that higher catchments drain later than lower situated catchments.



Die approbierte gedruckte Originalversion dieser Diplomarbeit ist an der TU Wien Bibliothek verfügbar
The approved original version of this thesis is available in print at TU Wien Bibliothek.

Zusammenfassung

Niederschlag zählt zu den wichtigsten Klimavariablen und ist von der GCMO mit Unterstützung der WMO definiert worden. Dies betont die Bedeutung von Forschungsfragen im Zusammenhang mit Schnee, insbesondere in Zeiten des Klimawandels. Weltweit sind zahlreiche Menschen auf Schmelzwasser aus höher gelegenen hydrologischen Einzugsgebieten angewiesen. Trotzdem gibt es bisher nur wenige Ansätze zur Analyse der Schneeschmelze mit Fernerkundungsdaten. Die bestehenden Ansätze konzentrieren sich hauptsächlich auf punktuelle in-situ Messungen als Groundtruth.

Ziel dieser Arbeit ist es daher, Sentinel-1 Rückstreudaten mit Oberflächenpegeldaten für vier aufeinanderfolgende hydrologische Jahre zu vergleichen. Dazu wurden zwei verschiedene Ansätze gewählt, um den Tag der Schmelzwasserfreisetzung für das jeweilige hydrologische Einzugsgebiet in der Schneedecke zu ermitteln. Diese Ansätze unterscheiden sich hauptsächlich durch die Schwellwertklassifikation von Nassschnee und in der Analyse der mathematischen Ableitung der jeweiligen Zeitreihe. Es wurden 35 verschiedene Einzugsgebiete analysiert und festgestellt, dass die Definition des absoluten Minimums der Zeitserie besser geeignet ist, um den Tag der Schmelzwasserfreisetzung zu bestimmen.

Zusätzlich wurde versucht, einen Hörschwellwert einzuführen, um den Unterschied des Tages der Schmelzwasserfreisetzung in verschiedenen Höhen zu untersuchen. Dabei zeigt sich in den Fernerkundungsdaten deutlich, dass höher gelegene Einzugsgebiete weitaus später Nassschnee erkennen als niedriger gelegene Einzugsgebiete.



Die approbierte gedruckte Originalversion dieser Diplomarbeit ist an der TU Wien Bibliothek verfügbar
The approved original version of this thesis is available in print at TU Wien Bibliothek.

Contents

1	Introduction	11
2	Background	13
2.1	Snow	13
2.2	Microwave Remote Sensing	17
2.2.1	Scanning Techniques and Interaction of EM-Waves in Media	17
2.3	Band segmentation	19
2.4	Sentinel-1 and SAR	20
2.5	Sensitivity of SAR-Backscatter Data to Snow	22
2.5.1	Snow Retrieval with SAR-Backscatter Data	24
3	Study Site and Datasets	27
3.1	Tiling System	27
3.2	Study Area	27
3.3	Meteorological Data	28
3.4	Backscatter Data	29
3.5	Digital Elevation Model	31
3.6	Water Level Data	31
3.7	Forest Mask	33
3.8	Landcover Classification	33
4	Methodology	35
4.1	Preprocessing the DEM	35
4.2	Snow Backscatter Identification	36
4.3	Wet Snow Classification	38
4.4	Snow Melt Dynamics using the Marin Method	39
4.5	Snow Melt Dynamics using the Beltramone Method	40
4.6	Preprocessing of hydrological data	41
4.7	Method Benchmarking	42
5	Results	45
5.1	Rain Response Time	45
5.2	Runoff Detection in a High Alpine Catchment	45
5.3	Runoff Detection in an mid-altitude Catchment	49

5.4	Enhanced Runoff Detection Using Land Cover Masks and Height Apportionment Techniques	51
5.5	Results for Hydrological Year 2018/2019	54
5.6	Results Benchmarking	55
6	Discussion	59
6.1	Response Time	59
6.2	Runoff Detection in a High Alpine Catchment	59
6.3	Water level investigation	59
6.4	Snow retrieval with Sentinel-1 backscatter data	60
6.5	Enhancing Beltramone Method	61
7	Conclusion & Outlook	63
	Bibliography	65
	Appendix	72

List of Figures

2.1	Behaviour of LWC (yellow) and SWE (red) in the melting phase of the snowpack (Marin et al. 2020).	15
2.2	linear, circular and elliptical polarization methods of a wave (Nave 2023).	18
2.3	Interaction methods of electromagnetic waves with media. a) Emission b) Absorption c) Diffuse Scattering d) Reflection. The image is inspired by Schanda (1986).	19
2.4	Simplification of SAR geometry (Lauknes 2004)	21
2.5	Relative dielectric permittivity of snow: left image represents the real part of the relative permittivity, right image shows the complex part of the relative permittivity. (Alonso et al. 2021)	24
2.6	Upper Image: relationship between snow wetness and backscatter coefficient σ_0 . Lower Image: relationship between snow wetness and contributor of surface scattering. The plot shows two surface conditions where the solid line has a RMS of 4mm (rough) and the dotted line a RMS of 1mm (smooth). (Shi et al. 1995)	25
3.1	Map of Austrian geology. Marked in light blue the Northern Calcereous Alps, which are highly susceptible to karst forms (Schubert et al. 2018).	28
3.2	Map of Austrian meteorological data. Marked in red the mean minimum and maximum temperature for each day between January 2017 and December 2021. Colored in blue the mean precipitation. Clearly visible are seasonal variations with higher precipitation rates in summer.	29
3.3	Normalized areas for backscatter coefficients β^0, γ^0 and σ^0 . With incidence angle as θ , A_β as reference area for slant range geometry, A_γ as reference area normal to the looking direction and A_σ as reference area on ground. δ_a and δ_r are the ground range resolution and the slant range resolution. And δ_a is the azimuth resolution. (Small 2011)	30

3.4	Hydropower stations in Austria. Most of the Austrian rivers are used for small hydropower generation. These over 100 hydropower plants account for more than 60% of the electricity produced in Austria. Image according to OEAV (2023).	31
3.5	Hydrological catchments in this study area. Each catchment represented in a different color. Marked in green the represented Tile over Tyrol (marked in red polygon)	32
3.6	HANSEN Global Forest Mask covering 36% of the Tile E048N015T1.	33
3.7	ESA-Worldcover Landcover map reprojected for Tile E048N015T1	34
4.1	Computed catchment for a certain outlet (red dot) in a specific catchment (green polygon).	37
4.2	Theoretical behaviour of a backscatter coefficient for morning (Descending, green) and evening (Ascending, blue) time-series. Influenced by LWC (yellow) and the SWE (red) evolution. (Marin et al. 2020)	39
4.3	a) example Timeseries of the VV-polarized timeline. b) smoothed timeline. c) First derivative of smoothed time series including positive anomalies (red) and negative anomalies (green). (Beltramone et al. 2023)	41
4.4	Watergauge and meteorological parameter for a common high alpine catchment	42
5.1	Backscatter contribution compared with meteorological parameter and water gauge data (VV-polarization).	46
5.2	Snowmelt dynamics via VH and VV polarized γ_0 representation and their derivatives. Split into ascending and descending pass. As soon the backscatter drops beneath the wet-snow threshold, the time series is plotted in red.	47
5.3	Elevation variation in the catchment. More than 50% of the catchment are at elevations higher than 2900m.	48
5.4	Snowmelt dynamics of catchment id: 201384 for the hydrological years 2018/2019 (upper image) and 2020/2021 (lower image).	49
5.5	Snowmelt dynamics compared with water gauge data for catchment id: 201574 for the hydrological year 2017/2018 shows no significant changes in the γ_0 time series.	52
5.6	Split γ_0 into heights above elevations higher than 1600m (upper image) and beneath elevations of 1600m (lower image).	52
5.7	Elevation steps for the Catchment id: 201574.	53
5.8	Runoff time for each catchment for the hydrological year 2018/2019 showing the time difference between the Beltramone method (red) and the Marin method (blue) compared to the water level rise observed in the insitu data	54
5.9	Schematic representation of the Marin Results (blue) and the Beltramone results (red) for each hydrological year separately compared to the melting detection of the water level data.	55

5.10	Snow heights were measured at three in-situ stations located at varying elevations. The winter of 2019/2020 exhibited lower snow accumulation compared to the other three winters. Data available at GeoSphereAustria (2023).	56
5.11	Schematic representation of the Marin Results (blue) and the same method including an additional forest mask (green) for each hydrological year separately compared to the melting detection in the water level data.	56
5.12	Map of all catchments. Those marked in red have no significant water level fluctuations. Marked in orange are catchments with 2 of the 4 years with no significant variation. The blue area indicates the distribution of limestone over the study area.	57
5.13	Schematic representation of the Marin method (blue) and the same method without the catchments showing no fluctuation (yellow) for each hydrological year separately compared to the melting detection of the water level data.	57
A.1	Meteorological comparison of the VH backscatter data for catchment 201384 shows a very cold period between the beginning of December until the start of February for the hydrological year 2018/20219.	73
A.2	Meteorological comparison of the VV backscatter data for catchment 201384 shows very cold days in December and at the beginning on January for the hydrological year 2020/2021.	73
A.3	Meteorological comparison of the VV backscatter data for catchment 201574 shows very cold days in February for the hydrological year 2017/2018.	74
A.4	Backscatter distribution for time series without 15 % forest cover shows only a slight drop of the signal in the wetting phase, therefore further investigation is needed.	74
A.5	The image provided shows the different catchments sorted by (1) outlet height, (2) catchment size and (3) mean distance to outlet. The values are sorted from minimal to maximal value, if the information is provided in the metadata. Information is not provided for the last 4 catchments.	75
A.6	Snowmelt dynamics for the catchment 201533 shows a very early beginning of the melting phases, whereas the increase in the water signal is detected a month later.	76
A.7	Runoff time for each catchment for the hydrological year 2017/2018 showing the time difference between the Marin Method (blue) and the Beltramone Method (red).	76
A.8	Runoff time for each catchment for the hydrological year 2018/2019 showing the time difference between the Marin Method (blue) and the Beltramone Method (red).	76
A.9	Runoff time for each catchment for the hydrological year 2020/2021 showing the time difference between the Marin Method (blue) and the Beltramone Method (red).	77

A.10 Runoff time for each catchment for the hydrological year 2017/2018 showing the time difference between the Marin Method (blue) and the Method without Forest pixels (green). 77

A.11 Runoff time for each catchment for the hydrological year 2018/2019 showing the time difference between the Marin Method (blue) and the Method without Forest pixels (green). 77

A.12 Runoff time for each catchment for the hydrological year 2019/2020 showing the time difference between the Marin Method (blue) and the Method without Forest pixels (green). 78

A.13 Runoff time for each catchment for the hydrological year 2020/2021 showing the time difference between the Marin Method (blue) and the Method without Forest pixels (green). 78

A.14 This catchment at the very north west of the study area shows high fluctuating water level. The Backscatter shows a clear drop of signal. The melting start in the water level data is not clearly detectable. 78

A.15 Schematic representation of the Beltramone Results (red) and the same Method without the catchments with no fluctuation (yellow) for each hydrological year separately. 79

List of Tables

4.1	Masked area due to layover and shadowing	37
4.2	Reference days for dry snow analysis for the relative orbits overflying the study area.	38

Acronyms

DEM Digital Elevation Model

EM Electromagnetic

ESA European Space Agency

InSAR Interferometric Synthetic Aperture System

LWC Liquid Water Content

MRS Microwave Remote Sensing

NIR Near Infrared

PLIA Projected Local Incidence Angle

RMSH Root mean square height

RTE Radiative transfer equation

S1, S1-A, S1-B Sentinel-1, Sentinel-1-A, Sentinel-1-B

SAR Synthetic Aperture System

SLAR Side-looking airborne radar

SWE Snow Water Equivalent

Chapter 1

Introduction

As a major source of life on Earth, the global water cycle is of vital importance to humanity. It consists of oceans, atmospheric water and water in the landscape. The oceans contain more than 95 % of the total amount of water on the planet. Glaciers, permanent snow cover, and ground water all contain more than 3% of the total amount of water. (Oki et al. 2004)

One-third of the Earth's land surface may be covered seasonally by snow, which together with sea ice make it one of the most dynamic components of the cryosphere and the most spread landcover type during the winter season. As the high albedo of snow strongly influences the energy balance and keeps the Earth's radiation budget in balance, snow is an essential climate variable (WMO 2023a; Dietz et al. 2012). The seasonal snowpack in the European Alps is the primary source of surface runoff and water supply in the adjacent lowlands. The ability to store water in the winter and release it in the spring is ideal for agricultural irrigation and is critical for hydropower production (Marin et al. 2020). Beside the hydrological importance, snow is also a major driver of the European economy. This is especially important for mountainous countries like Austria, where winter tourism and energy production are deeply intertwined and have a long-standing tradition. Hydropower plants generate over 65% of Austria's electricity, making them a crucial component of the country's energy production. Consequently, the melting of snow becomes a crucial factor in the ecosystem, emphasizing the significance of the snow-covered area (Buchelt et al. 2022). More than 2880 hydropower plants are feeding into the electricity grid of Austria (B. Wagner et al. 2015). The water discharge in Austria begins in early spring at lower sites and lasts until May or June for higher alpine regions. Between July and September the water discharge is still high due to melt of glacier ice (Marin et al. 2020; Baggi et al. 2008).

In most cryospheric studies one critical variable is the estimation of seasonal snow melt (Beltramone et al. 2023). Snow covered areas are often in remote and inaccessible areas, making in-situ studies and measurements to an expensive, time-consuming and dangerous expedition. In spring, wet and unstable snowpacks pose a high risk of wet snow avalanches (Beltramone et al. 2023; Baggi et al. 2008). Moreover, in-situ measurements only provide limited area information.

Detecting snow events with remote sensing data is a common approach to investigate remote areas without direct interaction with the snowpack or time consuming fieldwork (Nagler, Rott, et al. 2016; Beltramone et al. 2023; Marin et al. 2020). The use of optical remote sensing data is common for the detection of snow cover extend, snow mapping or improving those parameter which were originally investigated by field measurements (Dietz et al. 2012; Nagler and Rott 2000). Microwave remote sensing provides the capability to detect information that is not visible in optical remote sensing data. Microwaves possess an appealing quality for snow mapping and the detection of wet snow events due to their sensitivity to roughness and dielectric constant. In addition to their capability to gather data during nighttime, microwaves can effectively penetrate through clouds, which is particularly advantageous in mountainous areas that are frequently shrouded by cloud cover. Specially for remote areas where field observations are rare it appears to be a useful tool.

Active microwaves are often used to gather information about the wetness of snow (Naderpour et al. 2018) and to receive snow cover and snow variations as shown in Wang et al. (2018).

Schwank et al. (2018) retrieves snow density with radar L-band to verify the observed in-situ data. Passive microwave sensors have the ability to acquire data on the depth of snow by measuring the brightness temperature (Liu et al. 2018). Additionally, the monitoring of snow events using C-band SAR technology is extensively employed for research purposes, as it is sensitive to the analysis of liquid water content (LWC), as demonstrated in previous studies (Pivot 2012; Buchelt et al. 2022; Marin et al. 2020; Lievens et al. 2019).

Chapter 2

Background

This chapter discusses snow parameters, microwave remote sensing techniques and the combination of both: the interaction of microwaves with snow covered areas. The introduction into snow, snow physics and runoff time is given in Section 2.1. Followed with a short introduction into microwave remote sensing in Section 2.2 with a focus on interaction of electromagnetic waves as well as sensor specifications in Section 2.2.1. Section 2.4 goes into detail of Sentinel-1 and SAR. The chapter is completed by sensitivity of SAR to snow in Section 2.5.

2.1 Snow

The hydrological cycle is the continuous water circulation of the hydrosphere. It is the motion of the water system consisting of evaporation, transpiration, condensation, precipitation and runoff. In the form of snow, it is particularly important as a reservoir in mountainous regions and plays a critical role in the Earth's climate as an essential climate variable (WMO 2023b). Snow is often considered as water towers of adjacent lowlands (Viviroli et al. 2007). Water from snowmelt is important for water resource management like freshwater supply, irrigation and hydropower generation (Koch et al. 2019).

The hydrological year in Austria commences on October 1st and concludes on September 30th of the subsequent year. In regions with high mountains, the majority of autumn precipitation occurs as snow, resulting in the highest discharge rates during spring and summer. The lowest discharge rates are typically observed in September.

Physic of Snow

To effectively model snow using SAR data, it is crucial to delve deeper into the physics of snow in order to understand the fundamental mechanisms at play. A snowpack is usually divided into several snow layers with different characteristics. The snow layers mainly differ in grain size, grain form and density of the layers (Sommerfeld et al. 1970a). Due to wind or temperature changes, the characteristics of the individual snow layers can change rapidly

leading to unstable snowpacks and further to avalanches. Therefore, it is of great importance to understand the structure of the snow layers. The density of recently fallen snow typically is around 100 kg/m^3 , depending on the temperature and moisture content of the snow (Lastrada et al. 2021). After some days, the snow settles and the density increases up to 300 kg/m^3 . During this process, the grain size decreases as the structure of the snowflake breaks into smaller pieces. The continuous transformation of the snowpack during the settlement is mainly influenced by the transportation of water vapor, which is predominantly determined by the temperature gradient (Sommerfeld et al. 1970b). Two distinct types of snow metamorphism can be distinguished: constructive metamorphism and destructive metamorphism. Constructive metamorphism means the recrystallization of the grains which only takes place if the temperature gradient within the snowpack is more than $1^\circ\text{C}/10\text{cm}$. The water vapor transfer from the warmer snow layer to the colder layers. One of those metamorphism is depth hoar, which usually forms when the snowpack is shallow and for a long time exposed to cold temperatures. This creates a strong temperature gradient within the snow layer compared to the warm ground. This persistent weak layer usually stays until the end of the snow season and forms grains with a size up to 10 mm. Destructive metamorphism is equilibrium growth. The grains change from crystals to round forms with decreasing grain size. This occurs solely if the temperature gradient is less than $1^\circ\text{C}/10\text{cm}$ (American Avalanche Association 2023; Lastrada et al. 2021).

The key variable used to quantify the amount of snow is the snow water equivalent (SWE). The volume of liquid water if one would melt the snowpack. One method to measure the SWE without melting the snowpack is, by weighing the snow mass. This can be done by installing snow pillows (Taheri et al. 2022). Another technique is to measure GNSS signals beneath the snowpack compared to GNSS signals above the snowpack. With the damping factor it is possible to calculate the SWE (Koch et al. 2019).

For getting a deeper understanding in the melting season, the liquid water content (LWC) of the snow is introduced. This describes the percentage of liquid water in the snowpack. The higher the LWC, the wetter the snowpack. It is of utmost importance to have knowledge about the onset of the melting season. This is because the melt water provides essential freshwater resources to the valleys. Additionally, this information can aid in the prediction of wet-snow avalanches and is also beneficial for hydropower generation. The melting can generally be separated into three phases (Dingman 2015):

- Surface moistening phase: the uppermost snow layer starts to melt due to the increasing air temperature and solar radiation, as well as heat exchanges or rain on the superficial layers.
- Ripening process: the snowpack becomes isothermal. As there is no further temperature change, the wetting penetrates through the snowpack until the maximum retention capacity of the pores is exceeded.
- Runoff phase/output phase: is the snowpack saturated, further energy input (in form of wet precipitation, solar radiation or high temperature)

produces melt water that cannot be retained. The water starts to drain.

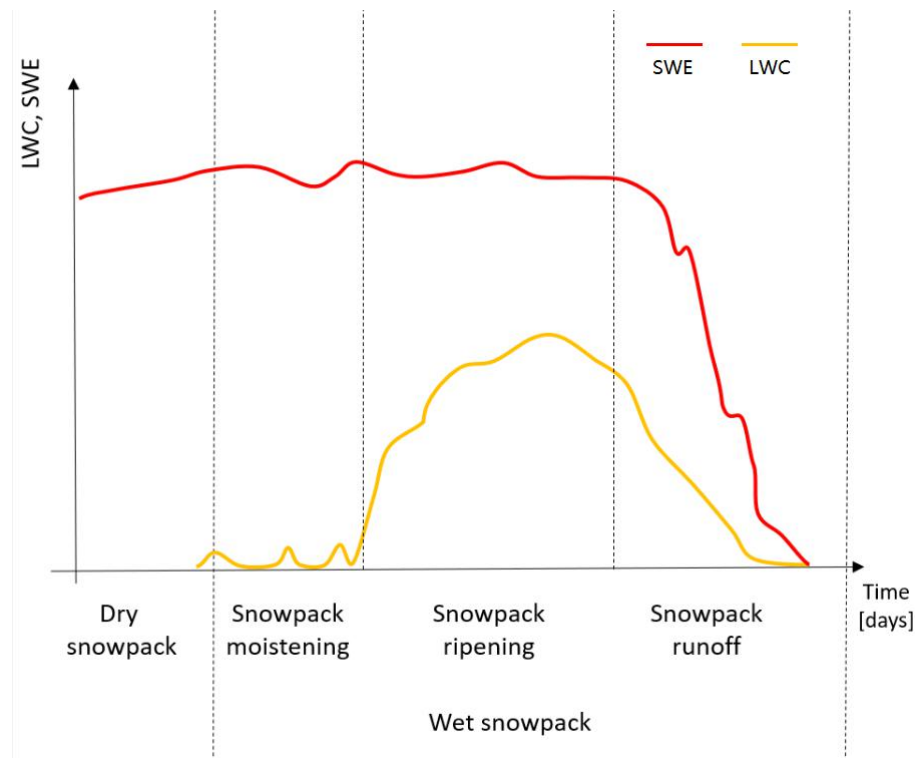


Figure 2.1: Behaviour of LWC (yellow) and SWE (red) in the melting phase of the snowpack (Marin et al. 2020).

The LWC and the SWE are most important to identify these three melting phases. The first slight increase of the LWC indicates the beginning of the moistening phase. The LWC decreases in the night due to refreezing effects and increases at day. This is illustrated in Figure 2.1. When the LWC starts to rise continuously, the ripening of the snowpack starts. This state holds until the maximum of the LWC is reached. Dropping LWC and SWE indicates the decrease of the snowpack by generating water runoff and introduces the runoff phase as shown in Figure 2.1.

Sometimes surface moistening phase and ripening phase can alternate before the final start of the runoff phase due to cold spell or fresh (dry) snowfall (Dingman 2015).

Runoff Time

Modelling runoff in mountainous regions is one of the most difficult hydrological processes to describe, as it is highly variable in time and space. It depends on a combination of climate, soil(moisture), geology and vegetation processes always being a mixture between surface- and subsurface runoff varying in different areas (Becker 2005).

If rainfall or snowmelt exceeds the infiltration capacity of the surface, runoff is generated. This runoff can be distinguished between

- surface runoff

- subsurface runoff

They differ highly in their response time. The response time is defined as the time between the runoff-generating event and the corresponding increase in the river below. Subsurface runoff can further be separated into interflow and baseflow (Barnhart et al. 2020).

Small catchments typically experience a relatively quick response time in terms of surface runoff, usually within a span of hours to days. However, interflow, on the other hand, can persist for a longer duration, ranging from several days to even weeks. Baseflow tends to last for months up to one year. Surface flow is mainly influenced by slope angles and the structure of the terrain. Less permeable areas like exposed rocks, saturated areas, urban areas or clay soils mostly produce surface runoff. Permeable areas such as vegetated landscape, with deep groundwater, never generate high overland flow rates, but rather subsurface runoff (Becker 2005).

Shallow snowpacks generally melt earlier in the year but at a slower rate due to the lower solar irradiance during early spring compared to late spring. Moreover, melting rates of snow are controlled by humidity, cloud cover change, energy balance and evapotranspiration rates. The pace of snowmelt-driven runoff is therefore the water input into the system, meaning the energy of radiance that drives the snow to melt. High snowmelt rates result in greater subsurface drainage and higher soil moisture (Barnhart et al. 2020).

Rain-on-snow events also affect the runoff time. Intense rainfall on a thin layer of snow results in significant runoff, whereas rain affecting deep and prolonged snowpacks leads to reduced runoff. The bottom line is that the snowpack plays a critical role in preventing extreme runoff events, even with heavy precipitation (Juras et al. 2021). Rain-on-snow events with short time differences between the rainfall and the snowpack runoff occur mainly in late spring or early summer. While events with slower time differences do usually not provide significant excess runoff (Würzer et al. 2016).

Rock glaciers provide a huge amount of water storage capacity due to their buffer capability. The presence of a fine-grained basal layer in a relict rock glacier enhances its water storage capacity, allowing for long-term storage. This emphasizes the significance of rock glaciers, as they can significantly impact the response time of alpine surface water. (T. Wagner et al. 2020; Winkler et al. 2016).

Blankinship et al. (2014) showed the influence of snowmelt on shallow soil water. Significant effects of snowmelt timing lasted 2 months in the shallow soil layer (0-15 cm depth). A reason for this finding might be the timing of snowmelt, evaporative demands and the soil water holding capacity. If melt occurs after evaporative demand increases, then the shallow soil can capture more of the slowly melting water, while water retention in deep soil remains limited by a low water-holding capacity.

2.2 Microwave Remote Sensing

Remote sensing as a technique to gather information of the Earth's surface, has the advantage of good coverage without costly and time-consuming in-situ field work. Especially remote areas that are hardly reachable can be easily analysed. The optical window, which encompasses the Near Infrared (NIR) range, displays a remarkable sensitivity towards plants and biological characteristics. Conversely, microwaves exhibit sensitivity towards the roughness and dielectric properties of an object, making them well-suited for extracting parameters as soil moisture, surface roughness and information about the dielectric constant. With a wavelength between 1 mm - 1 m microwaves can penetrate clouds and acquire scenes independent of illumination conditions.

2.2.1 Scanning Techniques and Interaction of EM-Waves in Media

Scanning Techniques

Satellites operating in microwave range can be distinguished between active and passive sensors.

Passive sensors are called radiometers. They are sensitive to a small amount of radiation, emitted by the object being viewed or reflected by that object with the radiation coming from a source other than the radiometer. Their primary purpose lies in measuring natural microwave emissions.

Active sensors are called radars. Radars have their own power source on board and emit radiation with a specific wavelength, enabling them to measure the backscattered pulses from objects located at a distance. These radars can be further grouped into classes: synthetic-aperture radar (SAR) systems, side-looking airborne radar (SLAR), scatterometers, altimeters, and meteorological radars. The received signal in SAR systems primarily relies on the roughness and dielectric property of the object, as well as the polarization (Ulaby et al. 2014).

Polarization

In most general form the electromagnetic wave is elliptically polarized. However, under specific circumstances this degenerate into a circle or line, leading to circular or linear polarized signal as seen in Figure 2.2. Circular polarization offers the benefit of diminished cross-polarized effects and occasionally exhibits improved penetration capabilities through vegetation. Whereas linear polarization are simpler to generate (Ulaby et al. 2014). Furthermore, differentiating between man-made objects and noise is more convenient. As a result, predominantly linear polarization is employed, particularly for inquiries related to snow retrieval (Patil et al. 2020; Ulaby et al. 2014). The polarization of linear polarized waves is determined by their direction of travel, which can be either vertical (V) or horizontal (H). Earlier

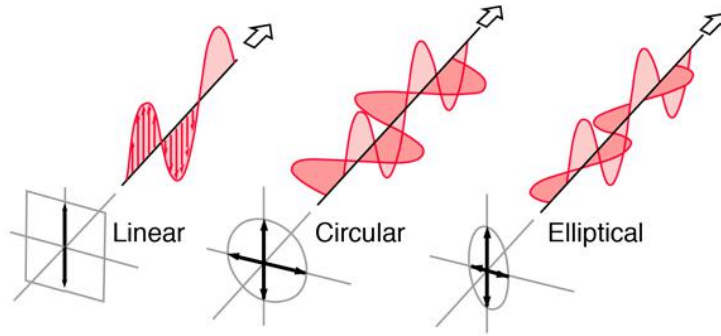


Figure 2.2: linear, circular and elliptical polarization methods of a wave (Nave 2023).

satellites received only single-polarized signals but modern satellite types have antennas that receive both co-polarized (VV,HH) and cross-polarized (VH,HV) signals. This leads to more image layers per scene and better discrimination of objects, as more information is given. Distinguishing between co- and cross-polarization may be important in retrieving surface roughness or moisture. Therefore, a combination of all signals tends to lead to better results (Irwin et al. 2018; Mouche et al. 2017; Lievens et al. 2019).

Dielectric Properties

How a certain material responds to an electric field is described by its dielectric properties. The permittivity describes the ability of a material to polarize its molecules in the presence of an electric field. Materials with high permittivity have a stronger interaction with media. They appear brighter in the radar returns. The permittivity (ϵ) is defined as:

$$\epsilon = \epsilon' + i\epsilon'' \quad (2.1)$$

where ϵ' contains for the real part, representing the lossless dielectric constant while the $i\epsilon''$ stands for the loss of energy (due to absorption).

Surface Roughness

If a surface is considered as smooth or rough, depends on the wavelength of the incidence wavelength. A surface is rated as smooth when the root mean square height (RMSH) is considerably smaller than the wavelength λ . The RMSH can be calculated via equation 2.2 where Z_i is the height at location i and \bar{Z} is the mean height over all n locations (Kirimi et al. 2016).

$$RMSH = \sqrt{\frac{\sum_{i=1}^n (Z_i - \bar{Z})^2}{n - 1}} \quad (2.2)$$

Interaction of EM-Waves in Media

Many models describe that the interaction of electromagnetic waves with media are based on the radiative transfer equation (RTE). Figure 2.3 demonstrates that radiation can be modified in 3 different ways. It can lose energy due to absorption and scattering mechanisms or gain energy due to emission.

- Emission: process in which the object radiates energy itself (thermal emission). See Figure 2.3 a)
- Absorption: process in which energy from the incoming EM radiation is absorbed by the object. See Figure 2.3 b)
- Reflection: process in which energy from the incoming EM radiation is reflected by the object
 - Specular Reflection: the energy is reflected in specular direction back to the source. Specular reflection is the main scattering effect on smooth surfaces. Figure 2.3 d)
 - Diffuse Scattering: energy is reflected in multiple directions. Diffuse scattering mostly occur on rough surfaces. Figure 2.3 c)

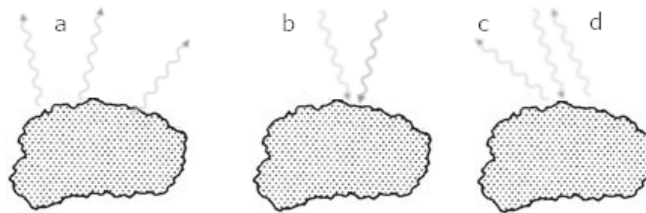


Figure 2.3: Interaction methods of electromagnetic waves with media. a) Emission b) Absorption c) Diffuse Scattering d) Reflection. The image is inspired by Schanda (1986).

The interactions between electromagnetic radiation and different surface features such as vegetation, water bodies, urban areas, or mountainous areas account for the satellite observations of the Earth's surface. These interaction elucidate the understanding of how satellite observations capture the characteristics of the Earth's surface. For a side-looking radar, diffuse scattering leads to higher backscatter return compared to specular reflection. For this reason, rough surfaces tend to appear brighter in the radar return compared to smooth surfaces.(Schanda 1986)

2.3 Band segmentation

As microwaves cover a wide span of the EM spectrum, they are further split into several band types. Common for microwave remote sensing are

- X-band: $\lambda = 2.4\text{-}3.75$ cm
- C-band: $\lambda = 3.75\text{-}7.5$ cm
- L-band: $\lambda = 15\text{-}30$ cm

Due to the different wavelengths X-band is mostly used for urban monitoring and for ice and snow monitoring (Rott et al. 2008; Gunn et al. 2015). C-band is primarily used in active radar remote sensing for areas with low to moderate penetration depths. The L-band has higher penetration depths due to its large wavelength and is therefore commonly used for vegetation mapping, biomass estimation and InSAR. (NASA 2023; Hamdan et al. 2014; Abe et al. 2020)

2.4 Sentinel-1 and SAR

Sentinel-1

Ever since the European Space Agency (ESA) launched the Copernicus Sentinel-1A and Sentinel-1B mission in 2014 and 2016 respectively, it has become feasible to achieve accurate temporal and spatial mapping of the entire globe. The satellites follow a sun-synchronous orbit with an inclination of 98° . With a 12-day repeat orbit cycle for each Sentinel-1 satellite, a temporal resolution of 6 days at the equator is reached when having two operating satellites, as both satellites are 180° apart from each other. This results in a revisit time of 3 days in Central Europe. The SAR instrument on board of the twin satellites is able to record information in four different acquisition modes, resulting in varying characteristics for different applications. Stripmap (SM), Interferometric Wide swath (IW), Extra Wide swath (EW) and Wave (WV) differ in swath widths from 80 km side looking up to 400 km side-looking. The active system on board provides vertical (V) and horizontal (H) polarisation and receive both V and H leading to images in VV, VH, HV, HH polarisation modes. (ESA 2023; Tsokas et al. 2022)

The IW is the main mode over land as it is a good tradeoff for most requirements. The terrain observation with progressive scans SAR (TOPSAR) is a technique to collect data in 3 different sub-swaths while constantly swinging the antenna. Compared to SM the azimuth resolution is lower as the target is shorter illuminated but results into a better slant range resolution (20×5 m for single look complex (SLC)) (Moreira et al. 2013). The products detected within the ground range (GRD) undergo a process of multi-looking and are subsequently projected into the ground range utilizing the WGS-84 reference system. This leads to a square pixel spacing of 10×10 m for IW and a resolution of 20×20 m. Phase information is lost due to the pre-processing steps. The spatial resolution is the measure of the ability to distinguish between two close scatterers. Pixel spacing is the distance between adjacent pixels in an image, measured in meters (ESA 2023).

Each satellite was designed for an operation lifetime of 7 years with reserves up to 12 years. Until recently both satellites were operating well, with S1-A exceeding its operation time. However on December 23rd 2021, the power supply of S1-B went down with no possibility of maintenance. Therefore, S1-A is currently operating alone leading to a coarse temporal sampling of 6 to 7 days in Central Europe. At the completion of this thesis there was no exact starting day announced for the S1-C satellite.

SAR

With the launch of Seasat in 1987 the first civil synthetic aperture radar (SAR) satellite commenced SAR systems in space. Dissimilar to optical data SAR Level-0 data do not give any useful information. Only after signal processing it is possible to extract imaging data.

The Sentinel-1 SAR instrument operates in C-band with a center frequency of 5.405 GHz (resulting in a wavelength of $\lambda = 5.55$ cm).

SAR systems image the world by utilizing the motion of the side-looking antenna to synthesize a large effective antenna, creating a virtual “synthetic” aperture, imaged in Figure 2.4. By doing so, SAR achieves a high azimuth resolution (across-track resolution) that is independent of the physical size of the antenna. This enables SAR to produce high-resolution 2D images and capture fine details on the Earth’s surface monitoring dynamic processes continuously and globally.

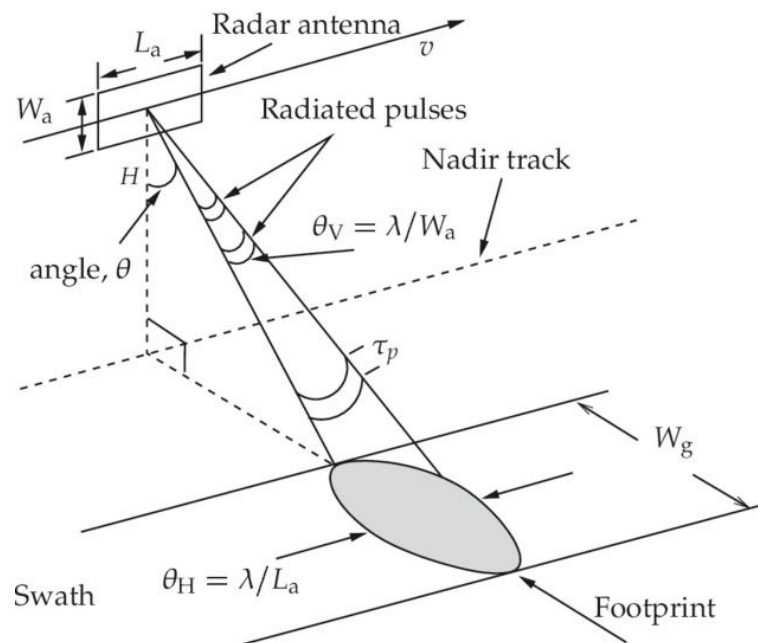


Figure 2.4: Simplification of SAR geometry (Lauknes 2004)

Range Resolution

The range resolution (S_R) of a radar system depends on the pulse-width (τ_p) and the speed of light (c).

$$S_R = \frac{c\tau_p}{2} \quad (2.3)$$

Meaning the smaller the pulse, the better the resolution. To overcome this problem, most modern SARs have a “chirp” technique, transmitting pulses linear over a certain frequency range and correlate it with the received pulse. This allows longer pulses with more energy without reducing the resolution. This pulse bandwidth (B) can be expressed as

$$B = \frac{1}{\tau_p} \quad (2.4)$$

leading to

$$S_R = \frac{c}{2B} \quad (2.5)$$

This shows, that the range resolution improves by having a wider bandwidth.

Azimuth Resolution

The azimuth resolution is not dependent on the frequency and range. However, it depends on the length of the radar antenna (L_a). For a real aperture radar the azimuth resolution (S_a) is described as (Raney et al. 1994):

$$S_a = \frac{\rho\lambda}{2L_a} \quad (2.6)$$

where ρ is the slant range and λ is the wavelength. If the object on the ground remains motionless and the satellite passes this object, it is possible to gather a synthetic generated antenna with a length equal to the along-track beamwidth ($= 2R_a$). The new azimuth resolution R'_a is given by

$$S'_a = \frac{\rho\lambda}{2R_a} = \frac{\rho\lambda L_a}{2\rho\lambda} = \frac{L_a}{2} \quad (2.7)$$

This means that the the resolution is independent of the antenna height and even improves, when the antenna length is reduced (Raney et al. 1994).

2.5 Sensitivity of SAR-Backscatter Data to Snow

MRS techniques detect changes in snow by taking advantage of the significant differences in dielectric properties between dry and wet snow. The variations are significant due to changes in permittivity caused by the liquid water content present in the snow.

Backscatter coefficient of snow-covered surfaces usually consists of contributions resulting from

- surface scattering from snow-air interface
- volume scattering from individual snow layers
- scattering mechanism resulting from the snow-ground boundary

The primary factor determining the dominant scattering mechanism in the C-band is the moisture content of the snow. The sensors frequency, incidence angle, polarization and other snow parameter such as grain size, grain shape and the roughness of the snow surface are important parameters for the backscatter retrieval of snow covered areas as well. (Marin et al. 2020; Tsai et al. 2019).

For dry snow, the signal easily penetrates the snowpack as ϵ'' of snow is low, therefore the surface roughness of snow can be ignored and the signal is almost insensitive to the remaining snow parameters. This results in signals that are most dependent on the scattering mechanism resulting from the snow-ground interface. Volume scattering becomes more important when the snowpack contains large snow grains like depth hoar or when thicker snowpacks are present. Scattering from the snow-ground boundary leads to backscatter signals looking similar to dry snow-free conditions, as the snow becomes almost transparent to the radar backscatter (Pivot 2012; Marin et al. 2020; Nagler and Rott 2000).

Snow Wetness Dependency on Backscatter Signal

The LWC plays an important role in the backscatter signal due to dielectric variations as mentioned above. As soon as the LWC increases, the upward reflection becomes increasingly dependent on the scattering mechanisms of the snow-air interface. As the snow becomes wetter, the LWC in the snowpack increases. This leads to an increasing dielectric contrast between the wet and dry snowpack. This highlights the possibility of mapping wet snow with C-band SAR backscatter. The behavior of the relative permittivity can be found in Figure 2.5. For C-band at 5.405 GHz, one can clearly see the variation of the real and complex part of the dielectric permittivity with increasing LWC. Wet snow leads to a decrease in permittivity due to a higher (complex) absorption coefficient (Buchelt et al. 2022; Nagler and Rott 2000; Marin et al. 2020).

Roughness Dependency on the Backscatter Signal

Surface roughness plays an important role in wet snow conditions. As the volume scattering effect can be neglected and the main contribution comes from surface-scattering. This means that for smooth surfaces there is a negative correlation between the backscatter signal and snow wetness. For rough surfaces the backscatter signal increases with increasing snow wetness. This behavior for the C-band is plotted in Figure 2.6 (Shi et al. 1995). An experiment about the roughness of snow was carried out by Nagler and Rott (2000). The idea was to artificially disturb the snow surface and compare it to an undisturbed area. The experiment was performed on a flat glacier

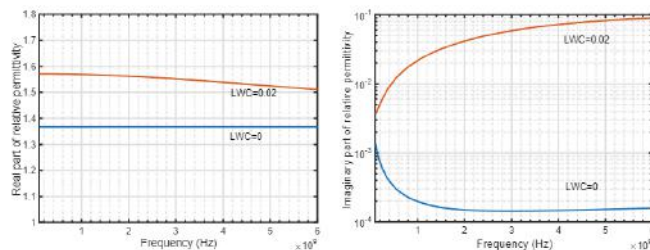


Figure 2.5: Relative dielectric permittivity of snow: left image represents the real part of the relative permittivity, right image shows the complex part of the relative permittivity. (Alonso et al. 2021)

located in the Austrian alps. It shows how the C-band backscatter signal is highly influenced by the roughness. The undisturbed area showed a mean backscatter $\sigma_0 = -19$ dB while the disturbed area showed a mean $\sigma_0 = -0.5$ dB.

2.5.1 Snow Retrieval with SAR-Backscatter Data

This section will shortly explain some methods for backscatter retrieval of snow covered surfaces. It shows the different possibilities to map snow parameter with remote sensing data.

Lievens et al. (2019) showed how snow depth can be retrieved from S1 backscatter data for a resolution of 1 km^2 based on temporal changes in the backscatter polarisation ratio VH/VV. The ratio is scaled to the range of snow depth measurements from the in situ sites. The cross-polarized σ_{VH} seems to increase with increasing snow depth. This new approach may be important for investigating total runoff or SWE analysis, and will also be of great importance for mapping runoff time and flooding.

Buchelt et al. (2022) described the mapping of snow cover and timing of snowmelt in arctic environments. The study identified the start of runoff, end of snow cover and snow cover extend with S1 observations using thresholds as well as derivatives of the time series in low vegetated areas. The results showed that roughness dependence occurs because surface roughness leads to depolarisation between cross- and co-polarised scenes, which is the reason for the incorrect assumption of the start of the runoff day.

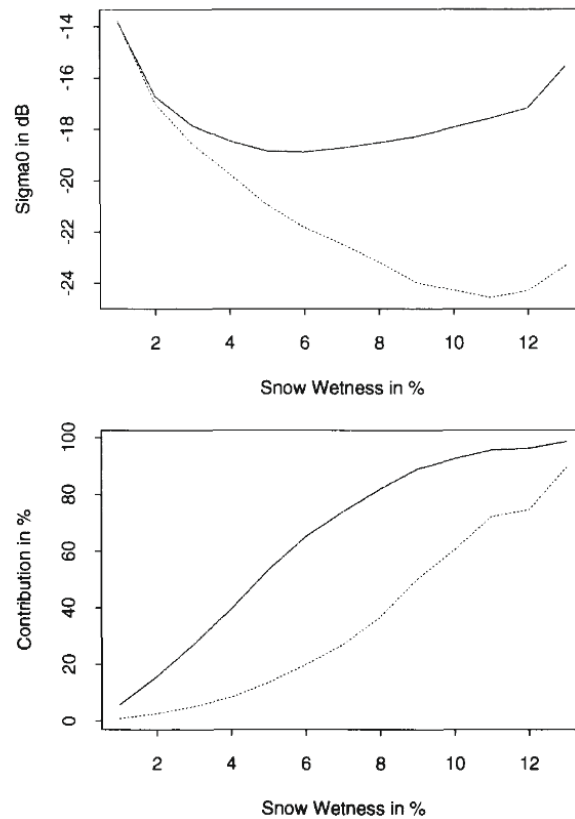


Figure 2.6: Upper Image: relationship between snow wetness and backscatter coefficient σ_0 . Lower Image: relationship between snow wetness and contributor of surface scattering.

The plot shows two surface conditions where the solid line has a RMS of 4mm (rough) and the dotted line a RMS of 1mm (smooth). (Shi et al. 1995)

Chapter 3

Study Site and Datasets

After having an introduction to the theoretical background, this chapter presents the study area and the data used in this thesis. The first Section describes the necessary tiling system (Section 3.1), as all data were collected for the size of the "E048N015T1" tile over Tyrol, Austria. This is followed by the specifications of the study areas (Section 3.2) and a the climatology of this high mountain region (Section 3.3). The next Section (Section 3.4) focuses to the γ_0 -backscatter data provided by TU Wien. Followed by Sections about the preprocessing steps of the DEM and the analysis of the water level data (Section 3.5 and Section 3.6). Forest Mask (Section 3.7) and landcover classification by the ESA Worldmap (Section 3.8) conclude this chapter. All data are available between 2017 and 2021. Leading to data for four full hydrological years.

3.1 Tiling System

The study site covers the western part of the Austrian province of Tyrol and refers to the tile "E048N015T1" of the Equi7Grid system introduced by Bauer-Marschallinger et al. (2014). This grid system allows an effective handling of remote sensing data by optimizing storage and processing of the spatial-grid. It is divided into 7 continental zones with individual projection. The "E048N15" refers to the azimuth equidistant projection with the coordinates $x=4\,800\,000$ m, $y=1\,500\,000$ m for the lower left corner. T1 refers to the tiling system. Tiling 1 means a 100 km grid extent for sampling between 1-16 m. (Bauer-Marschallinger 2015).

3.2 Study Area

The area of interest is the given tile clipped to the borders of Tyrol, Austria. This gives a total area of 6202 km^2 , which covers about half of Tyrol. The study site is located in the eastern alps with steep valleys. The main-valley Inntal is oriented in west-east direction with the capital Innsbruck at a height of 570 m.a.s.l. The entire region is characterized by mountains, reaching

heights of up to 3700 m above sea level. Particularly in the southern part of the study area, namely Kaunertal, Pitztal, Ötztal, and Stubaital, these mountains soar to over 3000 m. The whole study area has high altitude differences and steep valleys which can be more than 2000 m. The highest peak is the Wildspitze in the Ötztal at 3768 m. Most of the side valleys are oriented in a north-south direction. Snowmelt typically commences in the late winter months within the valleys and persists until the onset of summer in the mountainous regions. The predominant tree species in this area are conifers and the timberline is around 2000 metres above sea level. The valleys themselves are predominantly characterized by agricultural and rural landscapes.

The region north of the Inntal is primarily characterized by limestone, as depicted in Figure 3.1. While gneiss is the major rock, prevailing mostly south of Inntal. Limestone is susceptible to chemical weathering, potentially

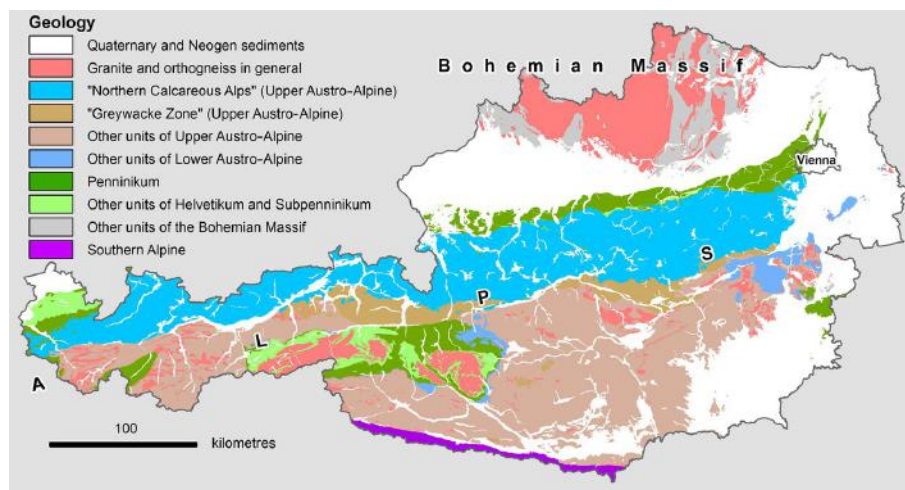


Figure 3.1: Map of Austrian geology. Marked in light blue the Northern Calcareous Alps, which are highly susceptible to karst forms (Schubert et al. 2018).

leading to karstification. This karstification tends to increase subsurface runoff, leading to less importance of stream gauging as significant peaks due to meltwater might be damped or lost.

More than 3000 rock glaciers cover over 160 km² of Tyrol. These permafrost landforms occur mainly in bedrock composed of paragneiss, orthogneiss and amphibolites exposed to the north (NO,N,NW) direction and provide a huge amount of water storage capacity due to their buffering capacity (Ribis 2013).

3.3 Meteorological Data

The climate in this tile is mostly characterized by cold winters with temperatures mostly beneath 0°C and short summers. Due to the topography, precipitation rates are relatively high and the temperature level remains moderate. To better understand the meteorological conditions, the SPAR-TACUS data set provided by GeoSphere Austria was used (Hiebl et al. 2015;

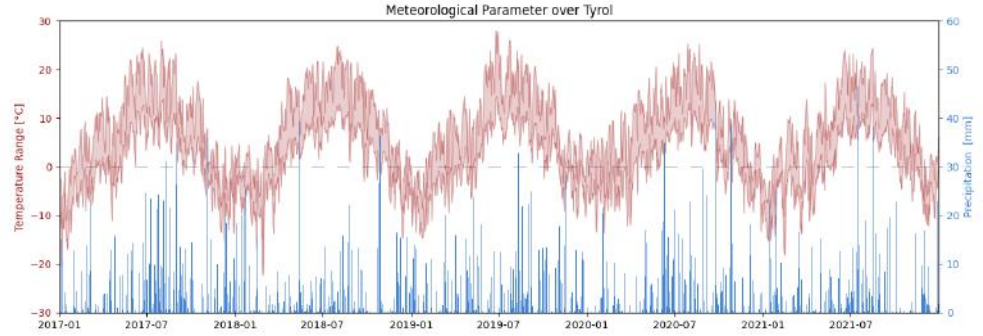


Figure 3.2: Map of Austrian meteorological data. Marked in red the mean minimum and maximum temperature for each day between January 2017 and December 2021. Colored in blue the mean precipitation. Clearly visible are seasonal variations with higher precipitation rates in summer.

Hiebl et al. 2017). This grid-based data set has a temporal resolution of 1 day and a spatial resolution of 1x1 km. Precipitation, minimum and maximum temperature are used to gather information about potential melting times and ice days. Ice days occur, when the maximum temperature never rises over 0°C. This becomes more important in Section 4.3. Figure 3.2 clearly displays the variations within a seasonal cycle. During the winter months, precipitation rates are lower compared to the summer months, and temperatures mostly remain below 0°C. The exception is the winter 2019/2020, which is relatively warm compared to the other tree winters. The mean temperature hardly drops beneath 0°C. In the summer months, higher precipitation rates and moderate warm summers prevail, with temperatures hardly exceeding 30 °C. (Hiebl et al. 2015; Hiebl et al. 2017)

3.4 Backscatter Data

Level-1 IW GRD data from Sentinel-1A and Sentinel-1B is used for snowmelt classification. The normalized radar cross section (NRCS) of a target represents the ratio of the energy scattered back to the satellite per reference area. The backscatter β is the ratio between the scattered power and the incident power at ground level $\beta = P_s/P_i$. While the backscatter coefficient β^0 gives the ratio per given reference area. A_β is the slant range plane resulting in β^0 illustrated in Figure 3.3. Since β^0 is not bound to an Earth model, it is not a very useful representation of a backscatter.

$$\beta^0 = \frac{\beta}{A_\beta} \quad (3.1)$$

The ground area as reference area is marked with a dashed purple rectangle in Figure 3.3. It is the tangent to an ellipsoid of the surface.

$$\sigma^0 = \beta \cdot \frac{A_\beta}{A_\sigma} = \beta^0 \cdot \sin\theta \quad (3.2)$$

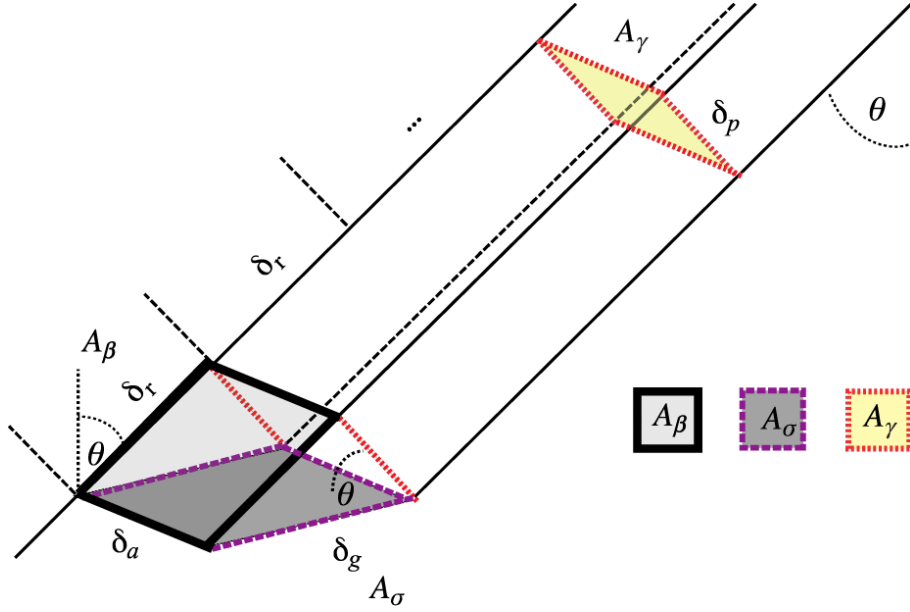


Figure 3.3: Normalized areas for backscatter coefficients β^0, γ^0 and σ^0 . With incidence angle as θ , A_β as reference area for slant range geometry, A_γ as reference area normal to the looking direction and A_σ as reference area on ground. δ_a and δ_r are the ground range resolution and the slant range resolution. And δ_a is the azimuth resolution. (Small 2011)

If the reference area is a plane perpendicular to the line of sight from the sensor to an ellipsoid of the ground surface, denoted A_γ , then the result is γ^0 .

$$\gamma^0 = \beta^0 \cdot \frac{A_\beta}{A_\gamma} = \beta^0 \cdot \tan\theta \quad (3.3)$$

The next step involves normalizing the real radar image to account for the radiometric effects due to topographic variations. This introduces radiometric terrain corrected estimates, denoted γ_{RTF}^0 , where r is the range image coordinate and a is the azimuth image coordinate (Small 2011).

$$\gamma_{RTF}^0(r, a) = K_\gamma \cdot \frac{\beta^0(r, a)}{\hat{A}_\gamma(r, a)} \quad (3.4)$$

K_γ is a calibration factor and

$$\hat{A}_\gamma(r, a) = \frac{A_\gamma(r, a)}{A_\beta} \quad (3.5)$$

Projected Local Incidence Angle

The projected local incident angle (PLIA) was available for each relative orbit direction. It represents the angle between the surface normal and the incidence angle of the radiation, projected into the range plane. The PLIA plays a crucial role in concealing regions that are impacted by layover and shadowing, particularly in mountainous areas characterized by steep valleys. Areas with PLIA greater than 75° and smaller than 15° are masked out.

25% for each orbit is masked out due to the orientation of the valleys and their slope.

3.5 Digital Elevation Model

The digital elevation model (DEM) was provided in the Equi7Grid by TU Wien. It was sampled to a resolution of 10x10 m to match the grid of the S1 backscatter data for the Tile E048N015T1. Section 4.1 provides a more detailed description of the preprocessing steps that should be taken into account to overcome any artefacts in the raw DEM, which may prevent its complete runoff.

3.6 Water Level Data

River gauge data provided by PegelAlarm ¹ is used to verify the melting start of the γ_0 backscatter data. Hydrografischer Dienst Tirol and Tiroler Wasserkraft AG gathered most of the used data for the years 2017 until 2021. In Austria, hydrological data goes back to 1893. The data includes

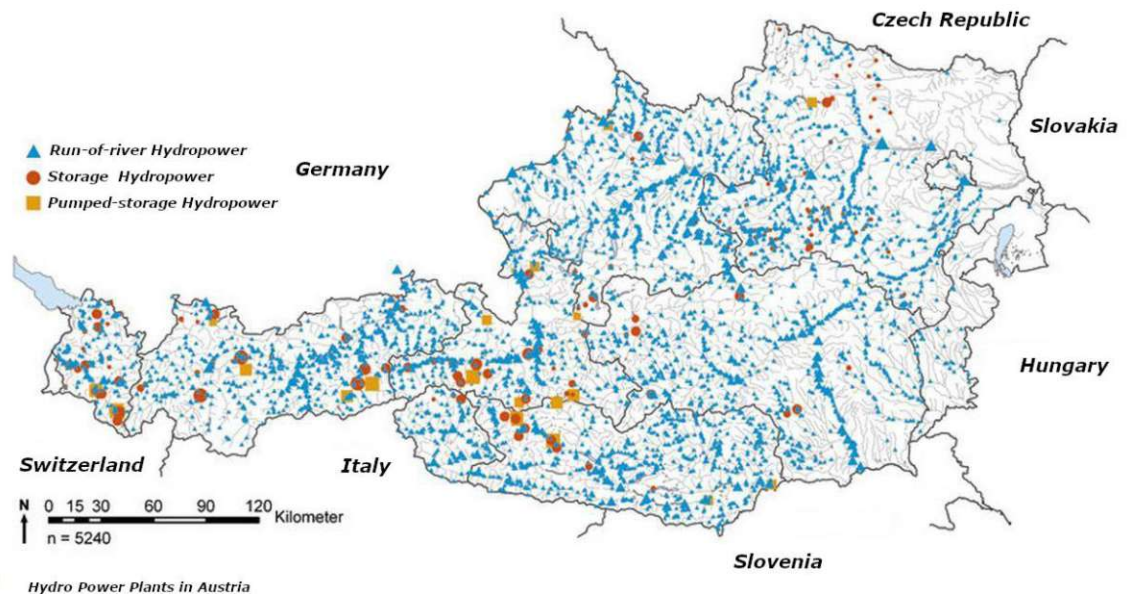


Figure 3.4: Hydropower stations in Austria. Most of the Austrian rivers are used for small hydropower generation. These over 100 hydropower plants account for more than 60% of the electricity produced in Austria. Image according to OEAV (2023).

parameters as air temperature, precipitation, drainage, rate of flow, ground water as well as suspended solids, water temperature and electrical conductivity. Currently, river levels are measured by placing an instrument on the bottom of the riverbed and using a pressure sensor to derive the current river level. It is important to note that changes in stream bed might

¹data used from <https://earlyfloodalert.com/>

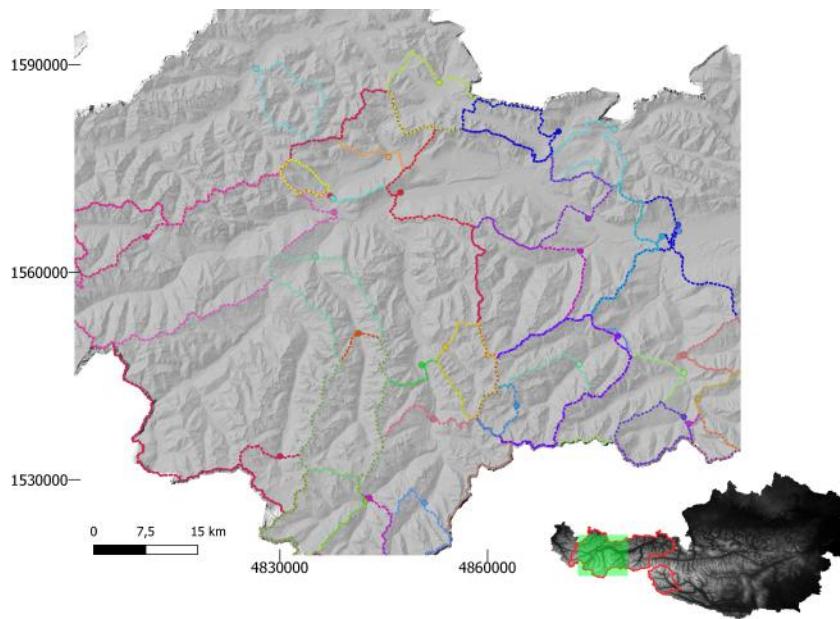


Figure 3.5: Hydrological catchments in this study area. Each catchment represented in a different color. Marked in green the represented Tile over Tyrol (marked in red polygon)

affecting the water level data permanently. In addition, the water level data represent only a small part of the river, which is very variable upstream and downstream due to changing river banks and widths. During the winter months, freezing of the gauges can lead to inaccuracies in the height of the water level data (*Hydro Online* 2023).

For the purpose of this thesis the hourly available water gauge data were averaged to a daily basis to filter out diurnal variations of the river gauge. For a better understanding of the data, the daily data points were delineated for each hydrological year. In Austria a hydrological year begins on 1st of October and ends on 30th of September of the following year.

It is important to note, that most of the Austrian rivers are obstructed by dams, or small run-of-river hydropower, leading to artificial water outlet. The amount of hydropower stations in Austria is imaged in Figure 3.4. This image shows that Alpine rivers are highly dominated by small hydropower plants.

For the whole study area 35 river gauge stations are available, contributing to 35 different catchments for snowmelt calculations. All hydrological catchments are shown in Figure 3.5, covering mostly the southern and western part of the study area. However, the northwest part, which includes the main valley Lechtal, has outlets that lead to Germany where no data were available for this work. The steps taken to obtain these catchments are described in section 4.1. The outlet height varies between 200 m above sea level and 1900 m. The catchments vary in size between 20.4 km² and 3372 km² contributing to a mean distance to the outlet between 100 m and 66 km.

3.7 Forest Mask

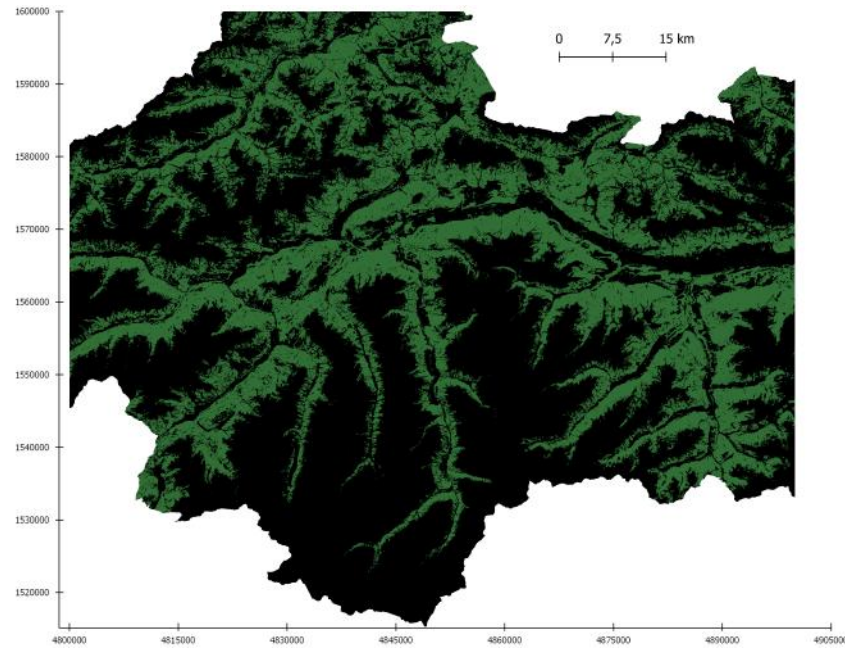


Figure 3.6: HANSEN Global Forest Mask covering 36% of the Tile E048N015T1.

Due to strong scattering of dense forest, the signal is mainly dominated by the vegetation and consequently compromises the sensitivity to snow parameter. As a result, the forest was excluded from the analysis. As input data serve the Hansen Global Forest Change dataset. It is reprojected to the Equi7Grid and subsampled to 10x10 m for a better comparison to the S1 backscatter data. This dataset based on time series analysis by Landsat images containing tree canopy cover for all vegetation taller than 5m. The dataset encompasses the years 2000 until 2019. Within the E048N015T1 tile, which is clipped to the boundary of Tyrol, forest areas account for approximately 36% of the total land coverage. The whole forest cover of the study area is presented in Figure 3.6. It is worth noting that the forest expansion adapts to the shape of the valleys, while regions above 2000 m are beyond the timberline and valleys close to the water are mainly human controlled. The drawback of this dataset is, that it has difficulties in recognizing sparse forest with tree coverage of less than 30% in one pixel (Schepaschenko et al. 2015).

3.8 Landcover Classification

The Landcover map "ESA-Worldcover" provides land cover classification with 11 different classes. With a 10x10 m resolution it is the first global land cover product for the years 2020 and 2021 based on Sentinel-1 and Sentinel-2 data provided in near real time (Zanaga et al. 2021). By first applying the HANSEN Global Forest Mask, the remaining landcover can

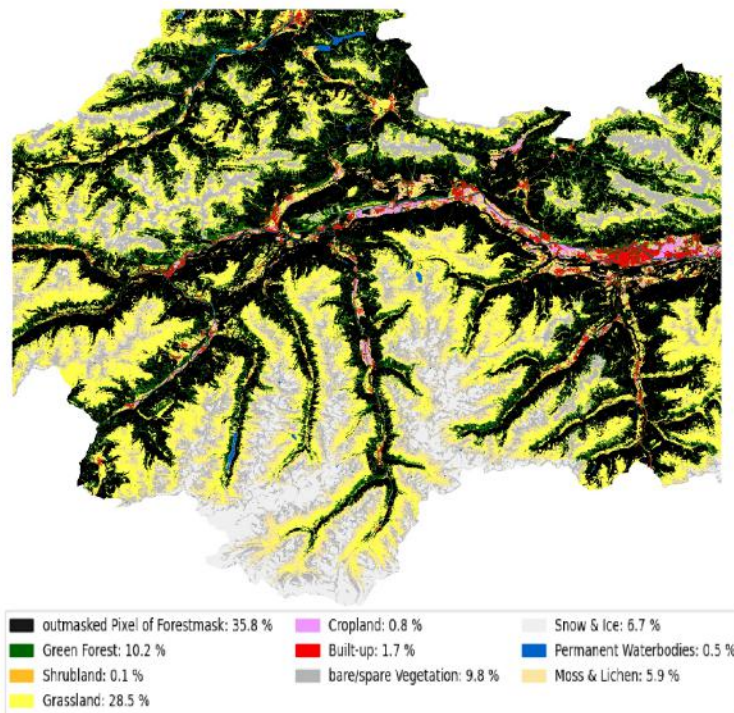


Figure 3.7: ESA-Worldcover Landcover map reprojected for Tile E048N015T1

be split into 9 remaining classes covering the study area. The forest that remains unmasked by the HANSEN Forest Mask accounts for 10% of the E048N015T1 tile, as depicted in Figure 3.7 in a green color. Grassland covers about 28%, spare vegetation 10%, snow & ice 7% and moss & lichen 5%. The remaining groups of built-up, shrubs, cropland and permanent waterbodies such as rivers and lakes cover the remaining 4%. The landcover classification of the study area is presented in Figure 3.7. It is clear that the west/east facing Inntal valley is densely populated and most of the southern part of the study area is covered by glaciers.

Methodology

This chapter is dedicated to the understanding of the methodology used in this thesis for depicting the melting cycle for each hydrological year. This is done by generating a melting start date to be compared with river level variations for each catchment separately. It starts with the section 4.1, which characterises the preprocessing steps for the DEM and the generation of the catchment areas for the water outlets. Followed by Section 4.2 describing the processing steps for the backscatter normalization, continuing to the Nagler's method of wet-snow classification in Section 4.3 and further developed in Section 4.4.

Section 4.5 describes the identification of snowmelt, using derivatives of the γ_0 time series. To compare these selected methods to in-situ data, the hydrological data is introduced in Section 4.6. This chapter concludes with a benchmarking of the methods used, presented in section 4.7. All computational steps are performed using Python 3.11. The Python packages used are mentioned in the respective sections.

4.1 Preprocessing the DEM

Preprocessing steps for the DEM are essential to create a hydraulically connected elevation model. Most DEMs contain artefacts due to the computation methods and downsampling to the desired resolution. The digital terrain analysis usually involves two essential steps, first using an iterative DEM preprocessing algorithm to remove pits and depressions and then using a recursive flow-direction algorithm to retrieve the flow accumulation and the catchments area (Qin et al. 2012). Those processing steps were done using the python package `pysheds`.

DEM Preprocessing Steps

First of all, a *fill pits* and a *fill depressions* method was carried out. A pit is defined as a single DEM grid cell with surrounding cells all of higher elevation. While a depression is a bowl-shaped area with multiple cells having no outlet. Pits are usually in flat areas and in floodplain regions creating discontinuities in drainage patterns and therefore highly influence

the hydrological response of a basin. These depressions and pits are often caused by errors in the DEM process and by real-world conditions. Therefore, DEMs need to be processed to remove these artefacts (Grimaldi et al. 2007; Qin et al. 2012). Pits and depressions are encountered by raising the cell height to the minimum height of the neighbouring cells. This results in a DEM where every pixel has an outlet and no depressions.

Raising cells elevation tends to create large flat regions. That is, cells where every neighbouring cell has the same height. This leads to misinterpreted flow paths with unrealistic parallel channels and other artificial features (Grimaldi et al. 2007). Therefore, a *resolve flats* method was carried out to overcome this problem. By introducing a small slope gradient to the flat areas, so each pixel has an outlet into an other pixel.

Catchment Retrieval

The catchment area of a water outlet is first generated using a flow direction algorithm. It determines how the flow drains from each given cell in the DEM into the neighbouring cell by using the D8-algorithm. This algorithm automatically extracts drainage networks using only the main drainage paths. It takes a cell and calculates the direction to the minimum of one of its 8 neighbouring cells (in N, NE, E, SE, S, SW, W or NW direction). If more than one neighbouring cell has the same minimum elevation, the flow direction is assigned to the most likely direction. (Qin et al. 2012; O’Callaghan et al. 1984)

The next step is to recursively calculate the flow accumulation from the flow direction for each cell. The flow accumulation is defined as how many cells flow through a given cell (Lindsay 2015). Meaning great values for river lines and low values for ridges as shown in Figure 4.1. By introducing the outlet point (marked in red), the entire catchment border (highlighted in green) can be obtained through flow accumulation. The provided figure illustrates catchment borders that align with the ridge of the mountains. The southern boundary of the catchment area is relatively flat due to the glacier, while the northern part near the outlet has steep slopes.

4.2 Snow Backscatter Identification

The management of large amounts of data, such as is the case in remote sensing, is a challenging task. A common way to manage this issue involves the utilization of data cubes. Data cubes are multi-dimensional arrays by representing data along a dimension of interest (for example along the dimension time). The python package yeoda provides datacube classes specially developed for using earth observation (Navacchi et al. 2022). The scenes available over the catchment area were recorded from 2 different orbit directions: ascending mode and descending mode. For both orbit directions, three different relative orbits pass over the study area. Those relative Orbits are O15, O44, O117, for the ascending pass and O95, O168,

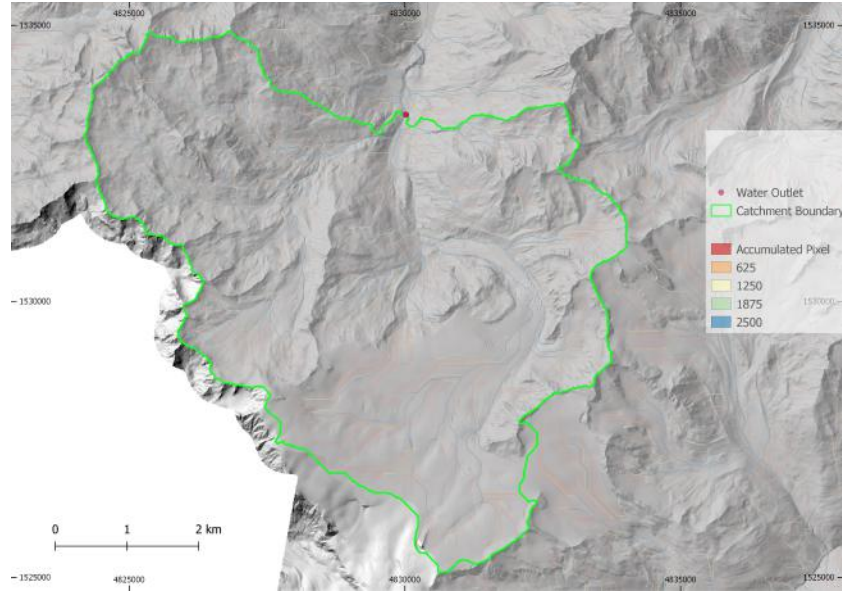


Figure 4.1: Computed catchment for a certain outlet (red dot) in a specific catchment (green polygon).

O66 for the descending pass.

relative orbit number	O15	O44	O66	O95	O117	O168
masked area	22.45%	30.2%	33.6%	20.7%	22.7%	23.8%
masked area (whole tile)	8.7%	1.3%	1.4%	6.3%	22.7%	23.8%

Table 4.1: Masked area due to layover and shadowing

First, the Hansen Global Forest Mask was applied, and layover and shadow masks were used to filter out areas with local incidence angles below 15° and above 75° . The outmasked area due to layover and shadowing effects can be seen in Table 4.1. It also gives an idea of how much of the whole study area is affected by the layover and shadow for each relative orbit separately, caused by the orientation of the valleys and the steep slopes.

For the ascending mode, the satellite travels to the north-northeast direction, while for the descending pass the orbit travels to the south-southwest. The acquisition times are about 5 pm UTC for the ascending mode and around 5am UTC for the descending mode. This is important to note, as the snow conditions are highly affected to melting/refreezing diurnal cycles so the time of acquisition needs to be considered (Marin et al. 2020). Due to steep slopes in the south-north oriented valleys in the study area, the orbit direction has a high influence on the time series because of shadowing effects. While many west-facing and some north-west-facing slopes are masked for ascending modes, descending orbits are blind to east-facing slopes. That is one of the reasons why all scenes have been split into ascending and descending orbit types.

For both orbit types the mean backscatter per scene was built over the whole catchment, separated into cross- and co-polarization. This leads to

4 different time series, distinguishable in polarization and relative orbit direction.

In order to capture the influence of the angle of incidence, a rolling mean was built over the amount of relative orbits for each orbit direction (ascending, descending) separately for each catchment.

4.3 Wet Snow Classification

To perform a wet snow classification according to Nagler and Rott (2000) and further developed by Nagler, Rott, et al. (2016), a ratio between the snow image and a dry reference image was calculated. The reference image should be either a snow-free scene or a scene with dry snow conditions. In the study area, the presence of high alpine terrain is constant, resulting in snow cover throughout the year. It is therefore extremely difficult to find snow-free days. Therefore, only scenes with dry snow conditions are included in the analysis.

Reference Dates for Wet-Snow analysis			
Date	Relative Orbit	Date	Relative Orbit
6.1.2017	117	23.1.2019	66
15.1.2017	66	24.1.2019	168
18.1.2017	117	25.1.2019	95
2.12.2017	117	10.1.2021	44
3.12.2017	44	15.1.2021	117
13.12.2018	168	16.1.2021	44
14.12.2018	95	27.1.2021	117
14.12.2018	15		

Table 4.2: Reference days for dry snow analysis for the relative orbits overflying the study area.

The selection of good reference images is essential for a good wet snow analysis. Single images might cause some problems due to changing soil moisture conditions affecting the backscatter. Calculating the average from the same relative orbits improves classification accuracy and also reduces speckle effects. For filtering these reference images, meteorological SPARTACUS-grid data with an spatial resolution of 1x1 km and a daily temporal resolution serve as input parameter. (Hiebl et al. 2015; Hiebl et al. 2017) If the maximum temperature of all pixels for the whole radar scene is below 0°C (indicating an ice day) and this condition holds for 3 days in advance, dry snow is assumed. The acquisition dates of the 15 reference scenes are in midwinter, between December and January. The exact dates can be found in Table 4.2, pointing out the warm winter 2019/2020 as no ice days can be observed.

If the ratio between the calculated reference scene and the given snow scene for a specific pixel is below 2 dB, wet snow is assumed. This method serves as basis for detecting snow melting phases described in the upcoming section.

4.4 Snow Melt Dynamics using the Marin Method

As the wet snow classification does not go deeper into the evolution of snow melting processes, an approach according to Marin et al. (2020) is introduced. For a hydrological year one single backscatter pixel is first influenced by soil moisture variations. Usually the first snow is wet or falls on a relatively warm terrain. This results in a wet snowpack with low backscatter values.

Either this snowpack melts and new (dry) snow falls later in the year, or the temperature drops resulting in a dry snowpack. This state holds for a few months in high alpine terrain. Before the melting phase begins, the time series remains constant, as the backscatter contributes mainly from the same snow-ground boundary. The LWC is low and the SWE rises continuously due to fresh snowfall during the winter. The dissimilarity in local incidence angles and the variation in illuminated areas caused by layover and shadowing effects account for the consistent offset between the ascending and descending orbits.

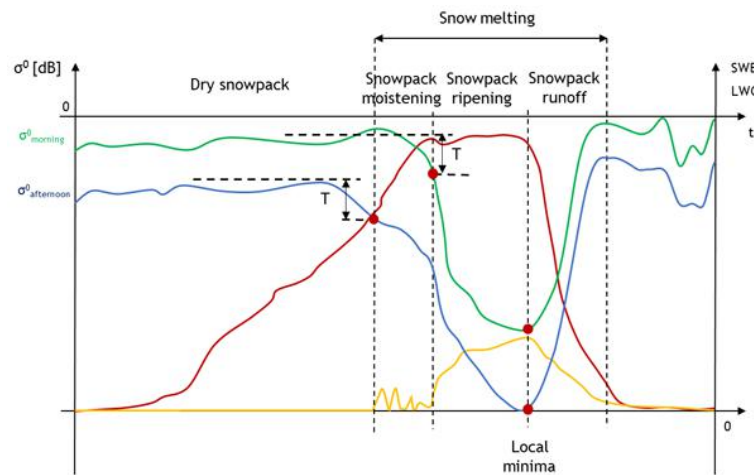


Figure 4.2: Theoretical behaviour of a backscatter coefficient for morning (Descending, green) and evening (Ascending, blue) timeseries. Influenced by LWC (yellow) and the SWE (red) evolution. (Marin et al. 2020)

At the beginning of the melting phase, the snowpack begins to incorporate liquid water into the topmost snow layer, leading to an increase in LWC and hence a decrease in the σ_0 signal (Marin et al. 2020). This drop is introduced by a threshold $t=2$ dB (according to the Nagler's method (Nagler, Rott, et al. 2016)) in the afternoon acquisition, as the upper snow layer is subjected to cycles of melting and refreezing every day and night, without affecting the morning signal. This indicates the start of the moistening phase shown in Figure 4.2 where the threshold is marked as a red dot.

When the morning recording falls below the 2 dB threshold, the ripening of the snowpack begins. At this point, wetting penetrates the snowpack and reaches the lower snow layers, contributing to an isothermal snowpack. The backscatter coefficient continues to decrease as the LWC continues

to increase. When the maximum pore retention capacity is exceeded, the runoff phase begins.

The minimum σ_0 is at the beginning of the runoff phase where the snowpack is saturated. This phase indicates the first drainage and consequently leads to a decreasing LWC and a drop in the SWE. The start of the runoff phase leads to an increasing backscattering coefficient. This may be explained due to increasing roughness, the change of snow parameter (such as grain size, grain shape and density) or the decreasing LWC. Moreover the snow runoff generates an intermittent snow cover inside a cells resolution, further leading to an increasing in the backscatter signal (Marin et al. 2020).

For this work, the method was adapted by calculating the mean of the time series related to the ascending mode and calculating the mean of the different time series of relative orbits relating to the descending mode, as six different relative orbits are used. A forest mask and a layover and shadow mask were applied. For each scene, the sum of all pixels for an entire catchment area was calculated. For a better understanding of individual catchments and individual backscatter behaviour of certain catchments, the time series was masked with certain landcover classifications and a height mask was applied. This has the advantage of showing snowmelt only at certain elevations and giving an impression of the runoff delay within a catchment for certain elevations.

4.5 Snow Melt Dynamics using the Beltramone Method

Beltramone et al. (2023) presents a novel approach to identify phasechanges in snow cover extent using Sentinel-1 data. The idea was to detect the seasonal snow accumulation and melting processes using time series derivatives and their positive and negative anomalies over Argentinean Patagonia. As input serve Sentinel-1 VV polarized time series for one specific descending pass. The beginning of the snowfall is indicated by the first negative anomaly (green vertical lines) presented in Figure 4.3. With this method it was possible to determine that the changes between bare ground and dry snow are significantly different.

The second negative anomaly shows the beginning of the wet snow phase due to the reduction in the backscatter. The positive anomalies represent the start of the runoff-phase. This detection is due to the shift from full snow covered areas to mixed land cover leading to an absolute minimum of the backscatter time series. All anomalies shown in Figure 4.3 c) represent values greater/smaller than one standard deviation of the first derivative.

For the study presented in this work, the method was slightly adapted. First a conversion of the time series from logarithmic to linear range was carried out before the derivatives are calculated. The Hansen Global Forest mask as well as shadowing and layover mask were applied. Moreover, the mean was built over the whole catchment and not just for single spots as presented in the study by Beltramone et al. (2023). For anomaly detection

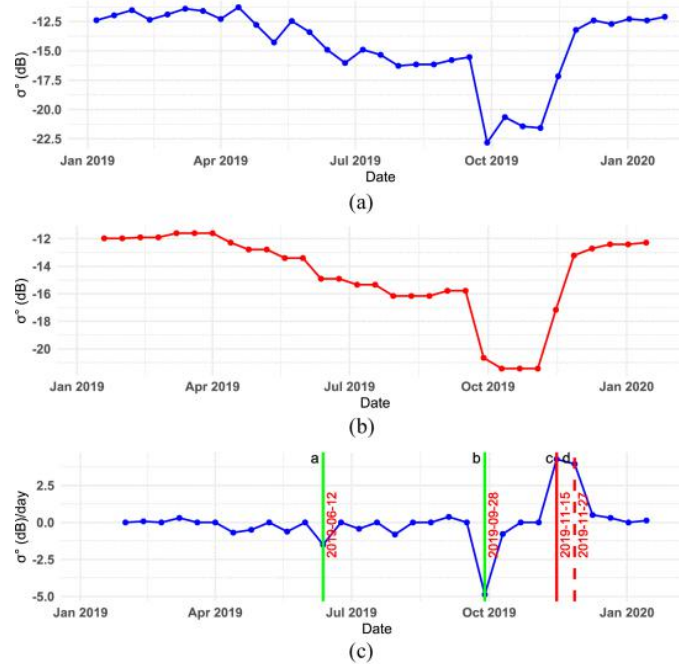


Figure 4.3: a) example Timeseries of the VV-polarized timeline. b) smoothed timeline. c) First derivative of smoothed time series including positive anomalies (red) and negative anomalies (green). (Beltramone et al. 2023)

the threshold was set to twice the standard deviation for a more robust detection.

4.6 Preprocessing of hydrological data

The hydrological data are available in an hourly resolution. In order to eliminate daily fluctuations, the average value was calculated for each day. The highest discharge occurs during the melting season in spring and early summer, primarily caused by the snow melting in elevated areas. Figure 4.4 illustrates the discharge pattern for one hydrological year. It can clearly be seen that the mean temperature of the whole catchment increases upon 0°C , followed shortly afterwards by a sharp rise in water levels. The hydrological data are available at hourly resolution.

Due to the presence of dams in most catchments, it is common to observe incorrect short high peaks in mid-December, as depicted in Figure 4.4. This rise does not represent the real runoff, but a false peak due to a refreezing gauge. The temperature range shown in Figure 4.4 is determined by calculating the average minimum temperature across the catchment area and the average maximum temperature for each day.

To compare the backscatter snowmelt events with a hydrograph, these wrong peaks due to the refreezing gauge need to be filtered out. For this purpose the precipitation data and the water level data are scaled via a minimum/maximum normalization. A peak detection was performed for both datasets to find high precipitation rates and filter high water level dates. The water level peak was determined by utilizing the width of the

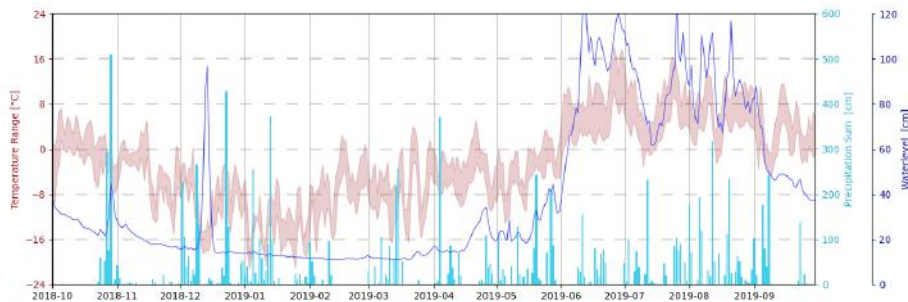


Figure 4.4: Watergauge and meteorological parameter for a common high alpine catchment

normalized signal, set at 80% of its height. Additionally, this peak must be sustained for a duration exceeding 2 days, during the melting period from February to July. The next step is to analyse the steepness of the water level slope. If it is rising very fast, having a gradient of more than 0.2 for the normalized time series, this day is introduced as start of water rise due to melt water.

A signal analysis was performed to calculate the response time for each catchment. Therefore, a cross-correlation between the precipitation and the water level data was calculated only for the summer months with temperatures higher than 1°C. The time lag between the rain event and the peak in the water level is introduced as response time for this certain catchment. It is important to emphasise that the calculated response time is strictly applicable to summer runoff and that the response characteristics can vary considerably between events within the same catchment. In addition, snow depth was found to have a strong influence on runoff time. The measurement of runoff timing is crucial, particularly when considering snow depth and its impact on the time lag to peak outflow and its interaction with snowmelt. (Kobayashi et al. 1985; Merz et al. 2003; Würzer et al. 2016)

4.7 Method Benchmarking

Several methods have been introduced to identify snowmelt from backscatter data: Firstly, a method using fixed threshold detection was used. (Nagler and Rott 2000; Nagler, Rott, et al. 2016). This method was further developed with a combined fixed threshold detection, involving the detection of the absolute minimum to capture the runoff phase introduced by Marin et al. (2020). The third method is a calculation of derivatives from the backscatter time series (Beltramone et al. 2023). According to Beltramone et al. (2023) the derivative method detects changes within the melting season in 92% of their study sites while the fixed-threshold method introduced in Marin et al. (2020) was only successful in 58% of the cases. It is important to mention that the anomalies were calculated using the derivatives from only one specific descending pass vertical polarized. The authors did not

mention why other relative orbits or the cross-polarization method were not considered.

Using non-fixed threshold methods offers the benefit of not relying on the selection of the optimal reference image and identifying an appropriate threshold. A fixed threshold is particularly problematic in forests, as the variation of the SAR signal is relatively small (Karbou, Veyssière, et al. 2021). Hence, a threshold function instead of a fixed threshold, may better account for signal variability with different land cover types and incidence angles. The use of optical data should be considered to identify only snow-covered areas (Karbou, James, et al. 2021).

Comparing the runoff days detected by these two methods with the start of the melt water rise in the water level data indicates how well the methods work.

Chapter 5

Results

This chapter enhances the results of the analysis. Initially the rain response time is outlined in Section 5.1. Next, some examples of different catchments are introduced in Section 5.2 and Section 5.3 and further developed in Section 5.4. The methods are developed by creating a land cover mask and dividing the backscatter into pixel-related heights above and below a certain threshold. All results for one specific hydrological year are listed in Section 5.5. This Chapter concludes by comparing both methods and adding additional investigations in Section 5.6.

5.1 Rain Response Time

The rain response time is estimated for all 35 water outlets. First, a comparison between the precipitation data and the water level data is accomplished. This was done by computing a cross-correlation function for the summer months, with the requirement that the temperature exceeds 1°C. The results indicate that the runoff time for each catchment was only one day, regardless of its size. The reason for this finding might be that the response time is considerably fast, within hours the precipitation influences the water level. Nevertheless, the water level data is adjusted to a daily resolution, which means that the peak can only be observed on the following day.

This response time is calculated for the summer response solely and assigned to the spring runoff as well. However, there could be significant fluctuations caused by the depth of snow and the saturation of the soil (Kobayashi et al. 1985; Juras et al. 2021).

5.2 Runoff Detection in a High Alpine Catchment

To differ the snow melting phases according to Marin et al. (2020), the method was applied to a high alpine catchment situated in the southwestern region of the study area within the Kaunertal. According to the metadata,

the catchment identified with id: 230300 is relatively small in size, encompassing only 54.3 km², having a mean distance to outlet of about 5080m and an outlet height at 1900m.

More than 55% of the catchments landcover relate to snow and ice, 16% to vegetation, 12% moss and lichen and 12% to grassland. The remaining 5% contribute to build ups and forest.

The examination of the water level data presented in Figure 5.1 (specifically

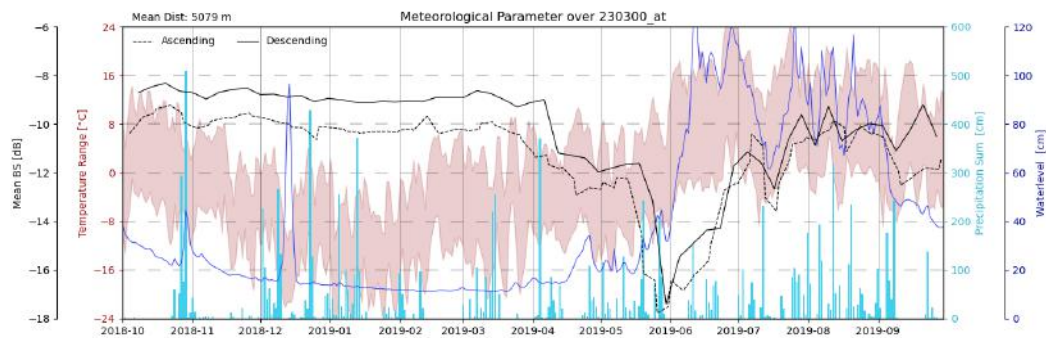


Figure 5.1: Backscatter contribution compared with meteorological parameter and water gauge data (VV-polarization).

highlighted in a deep shade of blue), show some strong peaks over the whole hydrological year 2018/2019. The first, at the end of October, appeared to be due to high precipitation rates across the catchment. In the lower elevations, precipitation occurs as rain, given the range of temperatures across the catchment in Figure 5.1. In addition, temperatures prior to the precipitation event were relatively high, resulting in a warm surface and subsequent rapid melting of the snow. The mid-December peak is noticeably higher than the first peak, yet there was no significant precipitation that could explain so much runoff. Furthermore, the temperature was relatively low during this period. This leads to the assumption that the gauge has frozen (as explained in Section 3.6), resulting in a false peak. During the remaining winter, the water gauge data are considerably low as precipitation falls as snow, resulting to a smooth and stable timeseries. In Spring, the first peak can be observed at end of April shortly after the temperature rises higher than 0°C. Followed by several minor peaks that correspond to fluctuations in temperature, the primary snowmelt occurred in early June. During this period, the average temperature was above 0°C, and there is a significant surge in the water level data. After the completion of snowmelt, the water level is primary influenced by precipitation events.

The VV polarized backscatter behaviour for the catchment is plotted as two black lines in Figure 5.1. The dashed line corresponds to the ascending pass, while the solid line represents the descending passes. The γ_0 shows no significant drop in signal during the initial precipitation event. This observation could possibly be attributed to the fact that the primary rain event occurred on October 28th and the next overflight was 5 days later on November 2nd. The absence of any changes in the backscatter data during the mid-December water rise event further supports the hypothesis that the

gauge was frozen.

By applying the methods described in Chapter 4, the melting phases shown in Figure 5.2 were derived. The backscatter data were split into ascending and descending mode and a rolling mean was computed for both orbit directions based on the number of relative orbits. Owing to the separation into VV and VH polarization, four time series for a single catchment per hydrological year were obtained. The ascending mode has slightly lower returns than the descending mode due to different illumination areas. Figure 5.2 denotes the four different backscatter time series. Ascending orbits were indicated by the color green, while descending orbits were denoted by the color purple. Those passes are further split into VV and VH polarization where the darker line indicates VH (dark green for the ascending orbit and dark purple for the descending orbit respectively) and VV is shown in light green/ light purple.

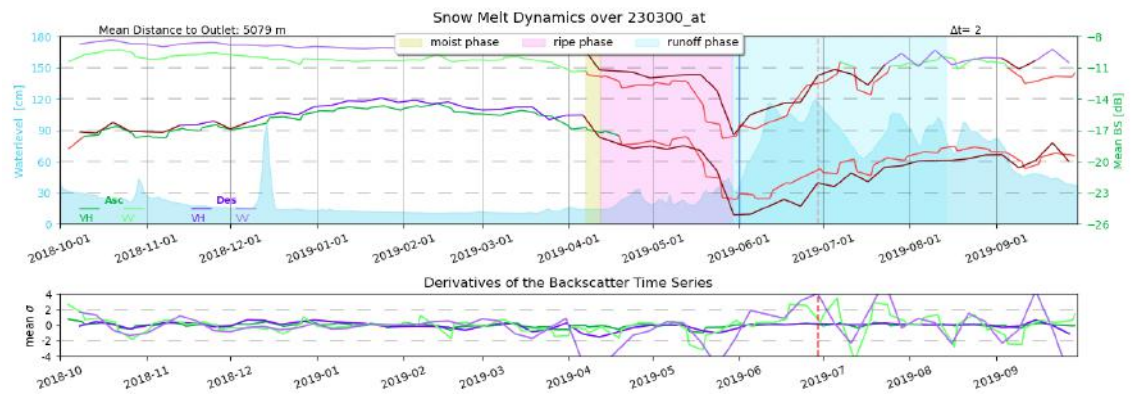


Figure 5.2: Snowmelt dynamics via VH and VV polarized γ_0 representation and their derivatives. Split into ascending and descending pass. As soon the backscatter drops beneath the wet-snow threshold, the time series is plotted in red.

As soon as the backscatter drops beneath the wet-snow-threshold of 2dB compared to the reference scene, the backscatter is colored in red (Nagler, Rott, et al. 2016). The blue vertical line indicates the start of the melting phase noticeable in the water level data. The lower plot shows the derivatives of all four backscatter time series.

When applying the Marin method one can observe that the γ_0 data remain constant until the melting phase begins mid of April. This moistening phase is introduced by a wetting in the descending pass and shortly after the wetting of the ascending pass indicates the start of the ripening phase. Those phases contribute to higher temperature rates (Figure 5.1) and a slight increase in the water level data.

This phase holds for over one month. End of May the absolute minimum of all four time series indicate the start of the runoff phase. The maximum retention capacity of the pores is exceeded, leading to the release of meltwater, which shortly afterwards contributes to a sharp rise in the

water level data. The time difference between the start of the runoff and the melting noticeable in the water level data (marked as a blue vertical line in Figure 5.2) is plotted on the upper left corner and indicates a delay of two days. Once the snow is completely melted, the backscatter data is primarily affected by precipitation events.

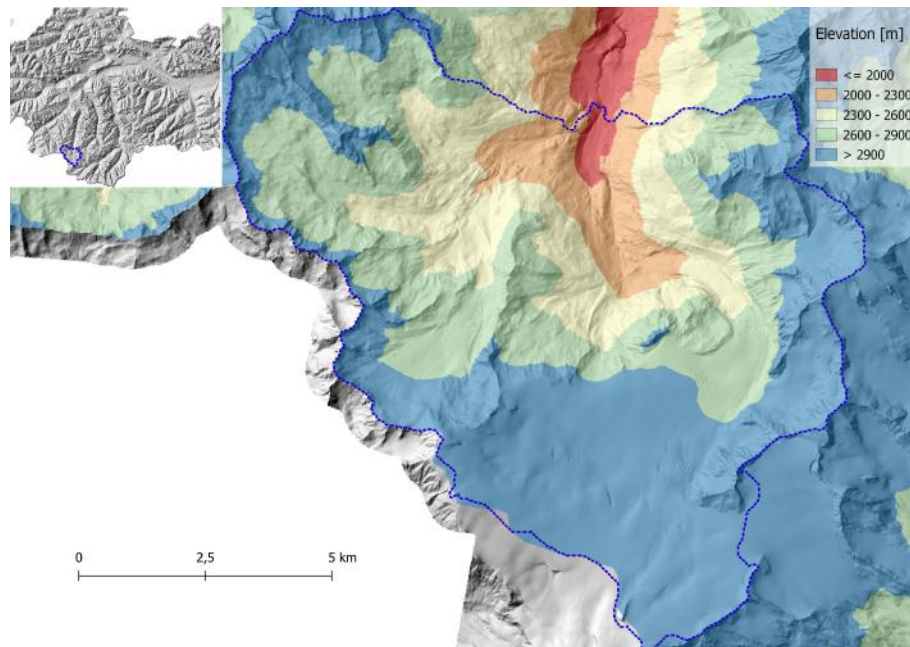


Figure 5.3: Elevation variation in the catchment. More than 50% of the catchment are at elevations higher than 2900m.

The Beltramone method reveals significant fluctuations in derivatives throughout the year, as shown in the lower plot in Figure 5.2. The descending VV backscatter signal exhibits two distinct declines in the derivatives. The initial negative anomaly should mark the start of the snow season, while the second negative anomaly should denote the start of the melting phase. It seems that the first negative anomaly is close to the start of the melting, detected with the Marin method. The second anomaly also lies within the melting season. When taking a closer look at the temperature data, there is a initial slight warming in April and a warming over the whole catchment in June. So the first decrease in the derivatives might indicate the snowmelt in the lower elevations, and the second drop might indicate the melting start in the higher elevated regions.

The Beltramone runoff-day was detected 30 days later compared to the Marin method. This leads to a later detection of 28 days compared to the water level perceptibly, depicted as a red dashed line over both plots. The derivatives across all time series indicate that during the winter snow cover, the values remain constant and stable, in contrast to the fluctuating values observed in the summer months.

Upon examining the water level data throughout the melting phase, it becomes evident that a slight increase in the water gauge can be observed

during the ripening phase, in the middle of April. This might be due to initial melting at lower elevations, noticeable in the whole catchment, by introducing the start of the melting phases seen in both methods. It shows that most of the catchment is at elevations higher than 2900m and only a small amount at elevations lower than 2300m.

5.3 Runoff Detection in an mid-altitude Catchment

The second example is a catchment located in the Ötztal, with the water station located in the Ötztaler Ache. This particular catchment, identified by the id: 201384, spans approximately 450 km² and has an average distance to the outlet of around 17 km. The drainage of this catchment is located in the village of Sölden, at an elevation of 1340 m. The maximum height in the catchment is the Wildspitze peak with 3768 m. The hydrological data are available between mid-May 2018 and end of 2021 with a gap between December 2019 and May 2020. This leads only to two full hydrological years - 2018/2019 and 2020/2021. Figure 5.4 shows the two time series for each hydrological year. 35% of the catchment contributes to snow & ice, about 20% each to grassland, spare vegetation and moss & lichen.

Looking at the upper plot in Figure 5.4 there is a slight peak in the

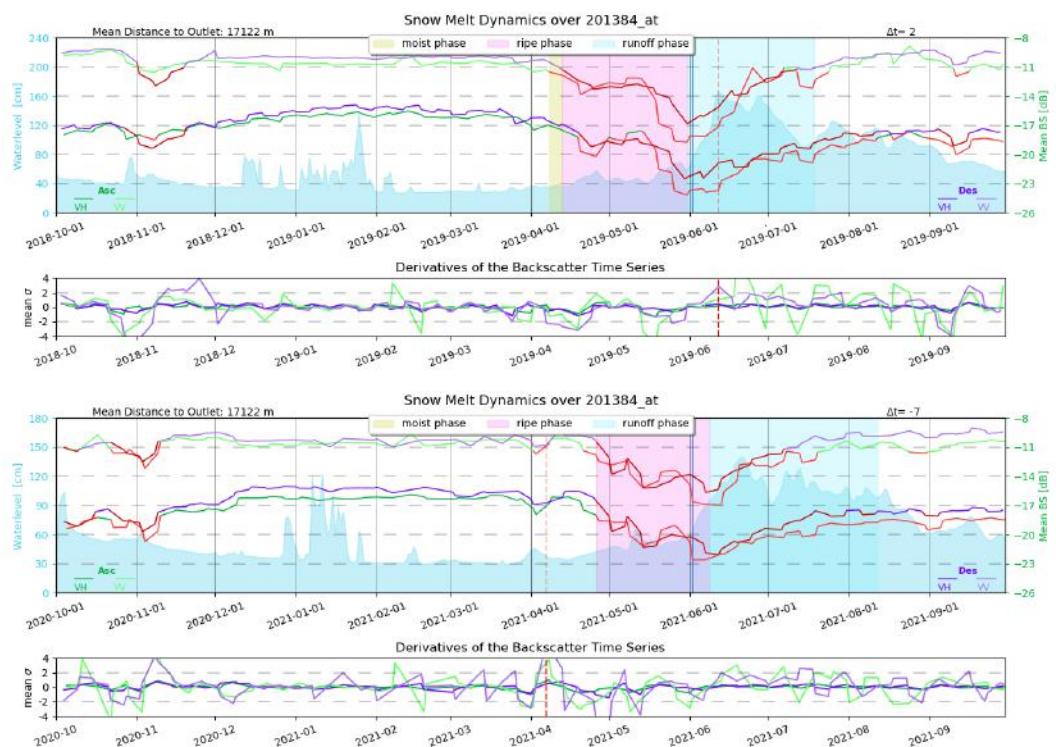


Figure 5.4: Snowmelt dynamics of catchment id: 201384 for the hydrological years 2018/2019 (upper image) and 2020/2021 (lower image).

water gauge at end of October, which could be due to the same rain event described in section 5.2. Both years show some short high peaks in the

water level data during December and January. Compared to the observed meteorological data, those months show very cold temperatures with a mean of -10°C (Figure A.1 and Figure A.2) for the days of the strong water peaks. This leads to the assumption that the gauge froze, indicating a wrong rise of water. Shortly prior to the outlet station, a small brook called Rettenbach drains into the Ötztaler Ache. The Rettenbach has a hydroelectric power plant, with controlled runoff behaviour. In both years, the initial spring water melt occur at the very beginning of June, resulting in a continuous rise of runoff for a duration exceeding one month.

The γ_0 data show a slight decrease in November for both years. This is usually the first snow in the season, which is wet or covers on relatively warm terrain - this results in a wet snowpack, generating this decrease of backscatter as shown in Figure 5.4.

The Beltramone method also encompasses the occurrence of initial wet snow event, particularly the distinct prominent negative peak observed during the hydrological year 2018/2019. During winter, the snow backscatter seems very smooth apart from a slight depolarization in February 2019 in the ascending mode. This depolarization is also distinctly evident in the derivatives method. The melting phases are first detected by the Marin method and one week later with the Beltramone method, showing a negative anomaly in mid-April. During the ripening phase, a slight increase in the water level can be observed in the ascending pass. This increase could be due to differences in the times and areas of illumination between the descending and ascending orbits. The start of the runoff phase for the Marin method is shortly before the melting can be detected in the water level data (2 days before). The Beltramone method, on the other hand, shows the start of the runoff phase when the water level is at its highest. The first snow of the coming winter season can also be seen, especially with the Beltramone method, which shows a clear negative anomaly in September 2019.

The second graph, shows the hydrological year 2020/2021. The Beltramone method shows a positive anomaly in November, which could indicate the first dry snow of the season or the increase in backscatter following the melting of the first wet snowfall of the season. This hydrological year shows a short depolarization in February as well where the ascending VV signal shows a short peak. In April, there is a slight decrease in the backscatter signal due a short warming (Figure A.2). This indicates the start of the runoff phase for the Beltramone method, nearly two months before the actual water rise is observed. The slight warming also comes with a slight increase in the water level data. The moistening phase for the Marin method is observed with the ascending orbit mid of April, shortly afterwards the drop of the descending orbit marks the beginning of the ripening phase. After the runoff start found with the Marin method, an increase of the derivatives can be observed as well but not clear enough for the automatic detection for the year 2020/2021.

Comparing Figure 5.2 with Figure 5.4 for the year 2018/2019, both graphs show a strong increase in water level data at the end of the melting phase, followed by a secondary peak about two weeks later. The water level data appear remarkably similar, and even the runoff phase seems to start around the same date for the Marin method. The initial negative peak identified by the Beltramone method should show the beginning of the snowfall in autumn. For the catchment id: 230300, the drop in the derivatives is not clear enough for an automatic detection. The second negative peak should show the beginning of the melting phase, visible in both catchments.

The method employed for the catchments depicted in Figure 5.2 and Figure 5.4 yields comparable outcomes to the Marin method. In both cases, there is a drop in derivatives during the autumn season. The second drop indicates the melting phase, similar to the melting phase found by the Marin method. The analysis shows that the Beltramone method performed less accurately than the Marin method during the runoff phase for both years.

It appears that the Beltramone method lacks robustness and is prone to even brief warming phases during the year. Other derivative timeseries, such as the VH polarization, were also analyzed but did not show significant improvements.

5.4 Enhanced Runoff Detection Using Land Cover Masks and Height Apportionment Techniques

Catchment id: 201574 is situated in the southeastern part of the study area, characterized by an outlet elevation of 1000 m. Spanning approximately 323 km², this catchment represents 5% of the entire study area and encompasses around 2.5% of the state of Tyrol. The catchment has a mean distance to the outlet of about 14 km. According to the ESA Worldcover classification, 60% of the catchment area is covered by grassland. After the Hansen Global Forest mask was applied, 15% of the area still contains remaining forests. Approximately 10% contains other forms of vegetation, and about 6% is covered by moss and lichen. The remaining part consists of snow and ice (6%) and built-up (3%).

Although, the catchment covers high alpine terrain, the γ_0 time series looks rather smooth with no clear drop of the backscatter signal (Figure 5.5). The time series data reveal that wet snow occurred for a limited number of days, and it was not feasible to identify the periods of snowmelt using the Marin method. This is due to the fact, that the ascending signals hardly drops beneath the threshold of 2dB from Nagler. Whereas the Beltramone method works very good for this catchment as the time delay between the runoff detection and the water level rise is 6 days. A very short high peak at the end of February was observed due to the freezing of the gauge as the temperature drops beneath -16°C (Figure A.3).

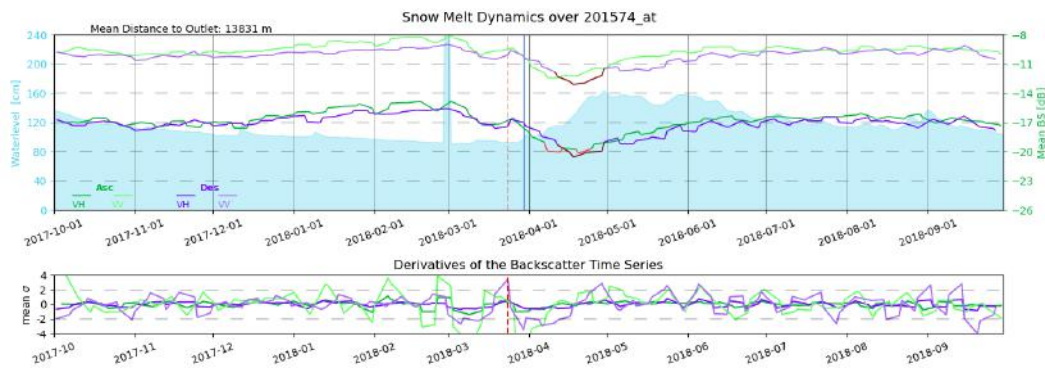


Figure 5.5: Snowmelt dynamics compared with water gauge data for catchment id: 201574 for the hydrological year 2017/2018 shows no significant changes in the γ_0 time series.

A further investigation was carried out to relate snowmelt phases with respect to the landcover classification based on the ESA Worldcover. Despite the application of the HANSEN Forest Mask, which was intended to exclude forested areas, it was found that more than 15% of the pixels still contained forest. Consequently, these pixels were masked out. However, this adjustment only resulted in a marginal enhancement of the data (see Appendix A.4). Another attempted method was to filter out various landcovers, but this did not yield any significant improvement in the findings. Therefore, the data were further analyzed by looking at the elevation steps within the catchment (Figure 5.7).

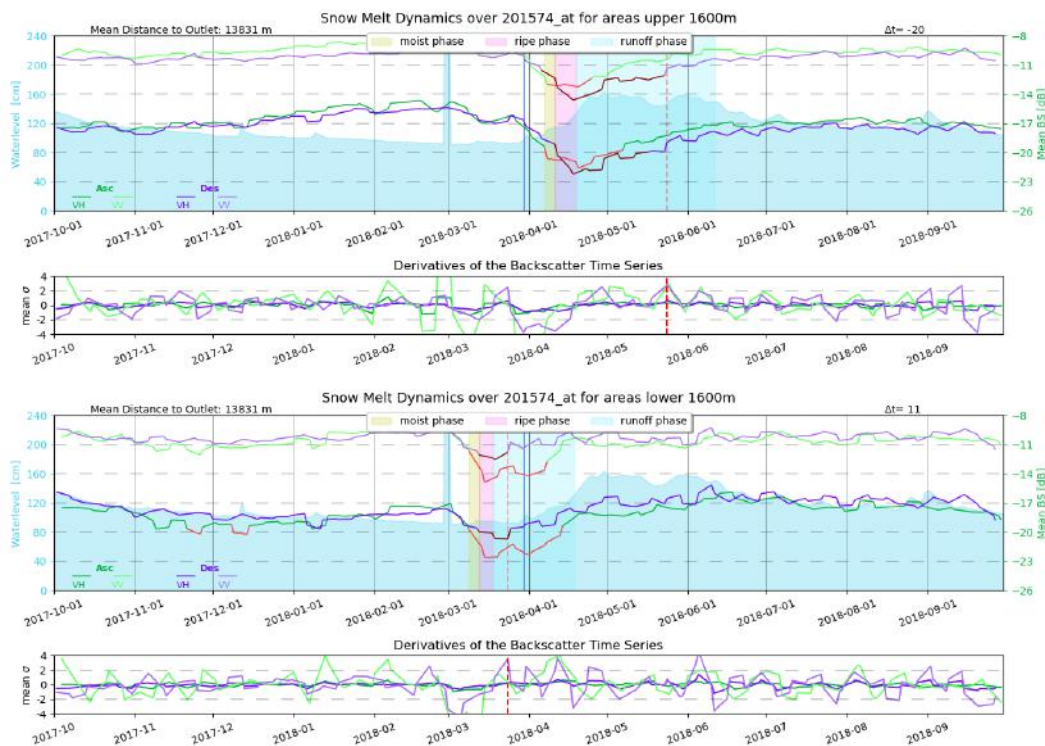


Figure 5.6: Split γ_0 into heights above elevations higher than 1600m (upper image) and beneath elevations of 1600m (lower image).

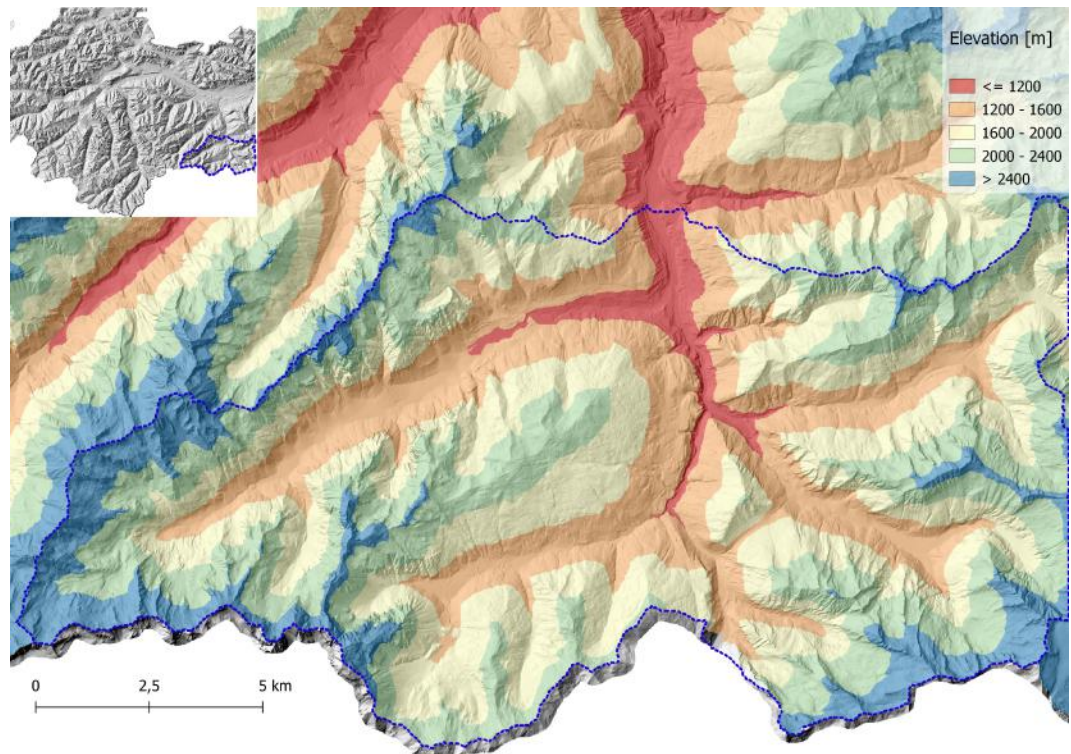


Figure 5.7: Elevation steps for the Catchment id: 201574.

The concept was to divide the backscatter based on specific elevation thresholds, aiming to gain a deeper insight into snowmelt patterns across varying heights. Particularly, it acknowledges that lower elevated areas may not always be covered by snow.

Figure 5.6 shows the time series of backscatter contributing to heights above 1600 m (upper image) and beneath 1600 m (lower image). The elevation threshold is visible in Figure 5.7 with areas below this threshold marked in red and orange. The Figure presents the possibility to automatically detect snowmelt using the Marin method when split in certain elevations. This method is only working for this catchment, when the remaining forest pixels are masked out as well.

The Beltramone method remains effective for regions below 1600 m. The start of the runoff phase occurs slightly earlier than the increase in the water level, whereas the detection of the melting phases according to the Marin method occur several days before the Beltramone method. The time series, which contributes to the pixel with elevations above 1600 m, illustrates the initiation of the runoff prior to its actual detection in the water gauge. The Beltramone method failed to promptly detect the runoff phase, lagging behind the observed water level fluctuations. The findings illustrate that the snow thaw occurs at an earlier stage in the season for pixels situated at lower elevations compared to those at higher elevations. Additionally, due to time differences, the behavior of various pixels cannot be observed when computing the mean over the entire catchment. However, there is a clear melting phase, especially for higher elevated pixels. One possible reason for the lack of significant changes in

water levels in the lower regions could be the shallow snowpack, which may have resulted in less clearly defined backscatter behaviour. However, it is uncertain whether this shallow snowpack had a significant impact on the water data.

5.5 Results for Hydrological Year 2018/2019

A total of 28 distinct catchments (Figure 5.8) were considered by aggregating all available hydrological data for the year 2018/2019, indicating the successful application of at least one of the methods in each catchment. The vertical lines indicate the time lag between the water level rise and the start of the runoff phase. Where the Marin method is colored blue and the Beltramone method colored red. A negative value indicates that the runoff day was detected after the rise of the water level in the in-situ data.

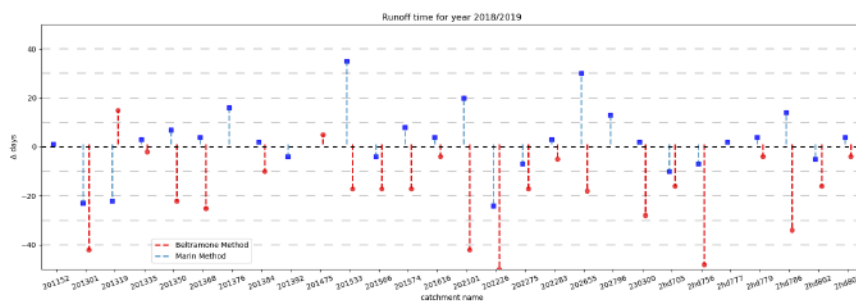


Figure 5.8: Runoff time for each catchment for the hydrological year 2018/2019 showing the time difference between the Beltramone method (red) and the Marin method (blue) compared to the water level rise observed in the insitu data

In the majority of the given examples, the Marin Method outperformed the Beltramone Method. This highlights the importance of using all available information, as demonstrated by the Marin Method, rather than relying solely on a single time series, as done in the Beltramone Method. In some examples only one of both methods worked. For the hydrological year 2018/2019, both methods were found to be effective in 22 catchments. However, in five instances, only the Marin Method proved successful, while in one case, the Beltramone method was the only method that yielded positive results.

There appears to be a potential correlation between the size of the catchment and the time delay (see Appendix Figure A.5), although there was no time difference detected for runoff time in the summer months. The Beltramone method proved ineffective in capturing data from catchments with ids: 201384, 201533, 2hd786, and 202226 due to the delayed surge in backscatter intensity during the later stages of the melting season. This delay indicated the end of the runoff phase in the Marin method. For catchment id: 201533 there was a false identification of the melting for both methods (Figure A.6). The Beltramone method exhibited a delayed identification of the runoff phase towards the end of the season, while the

Marin method detected it excessively early. Despite attempting various landcover masks and dividing the data into distinct elevation intervals, the results did not exhibit any enhancement.

5.6 Results Benchmarking

Figure 5.9 shows the comparison between the Marin method and the Beltramone method over all available hydrological years.

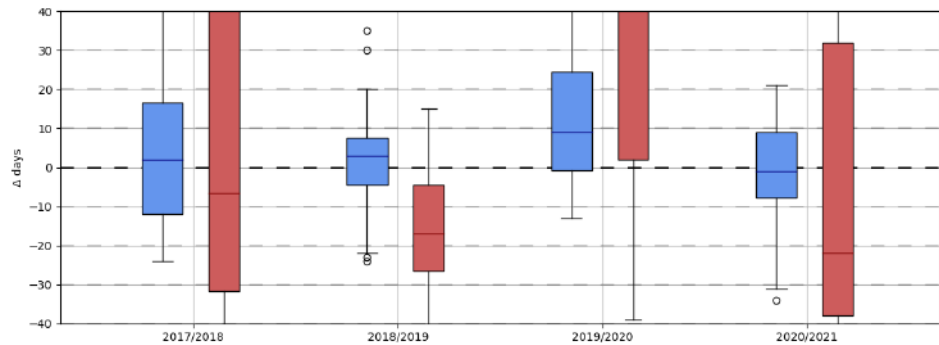


Figure 5.9: Schematic representation of the Marin Results (blue) and the Beltramone results (red) for each hydrological year separately compared to the melting detection of the water level data.

The boxplot depicts the spreading of both methods compared to the rise of the water level data. A closer look at the median distributions shows that the results of the Marin method are within $\Delta days = 5$ whereas the Beltramone method shows highly varying distributions with a median reaching over $\Delta days = 40$. Overall, the Marin method is the more favorable choice compared to the Beltramone method due to its higher likelihood of producing reliable results and its consistent effectiveness. In contrast, the Beltramone method often fails to identify any notable changes. However, there are instances where the Beltramone method succeeds while the Marin method falls short, but these occurrences are limited and are shown in Section 5.4. The data shown in Figure 5.9 clearly demonstrates that for the hydrological year 2019/2020, both methods produced a significantly high median, while the runoff detection method performed exceptionally well in the other years. A comparison of the average snow height in Figure 5.10 at three specific stations reveals that the winter of 2019/2020 had less snow than the other three years, specially for lower elevations.

As stated in Section 5.4, a technique for enhancement involved utilizing the ESA Worldcover Classification to conceal the remaining forest pixel. Figure 5.11 shows the boxplot with the outmasked remaining forest pixels in green. It is evident that the extent of spread in the unmasked outcomes is slightly reduced in comparison to the original Marin method. In the year 2019/2020, there is a decline in precision, whereas for the remaining years, there is a marginal improvement.

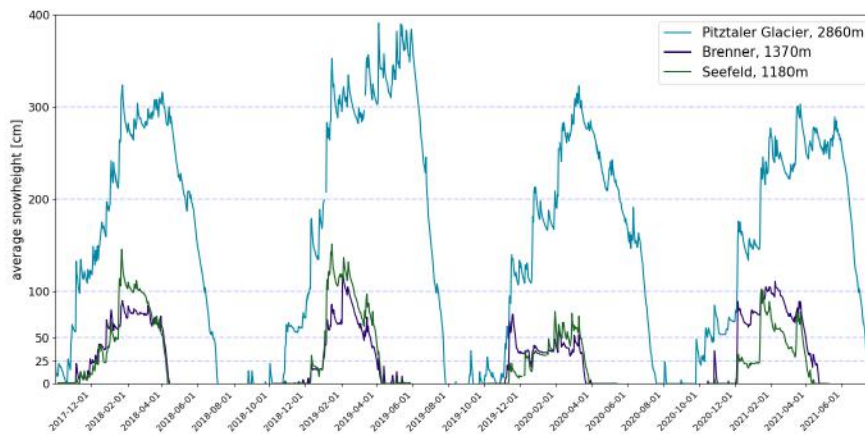


Figure 5.10: Snow heights were measured at three in-situ stations located at varying elevations. The winter of 2019/2020 exhibited lower snow accumulation compared to the other three winters. Data available at GeoSphereAustria (2023).

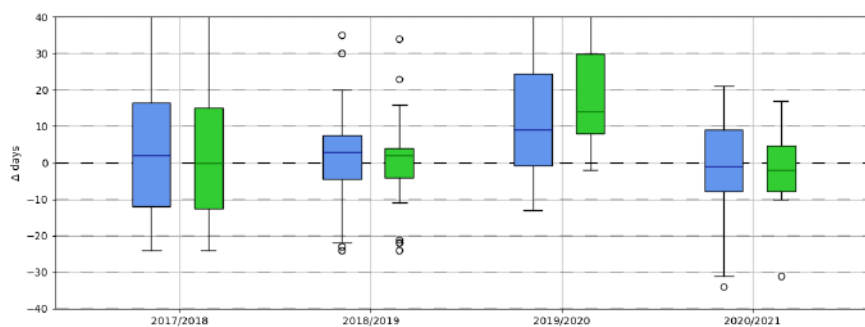


Figure 5.11: Schematic representation of the Marin Results (blue) and the same method including an additional forest mask (green) for each hydrological year separately compared to the melting detection in the water level data.

Figure A.7 - Figure A.13 show the scatter plots for all years separately. First, the comparison for the Marin and Beltramone method (Figure A.7-Figure A.9) is shown and followed by the results for the Marin method compared with the Marin method, including outmasking the remaining forest pixels (Figure A.10 - Figure A.13).

Some catchments do not have significant water level fluctuations. Consequently, these catchments are excluded from the analysis due to the inaccurate estimation of the duration of the water rise. A map (Figure 5.12) shows the position of those catchments. The distribution of the catchments that do not have significant fluctuations in the water level is conspicuously related to the appearance of limestone (marked in blue). Limestone is susceptible to build karst forms. Only one catchment (id: 202226) embedded fully in limestone contributes to outlets with high fluctuations and therefore

marked in green. The fluctuations of this catchment have repeating short high oscillations, indicating no clear start of the melt water release (see Appendix A.14).

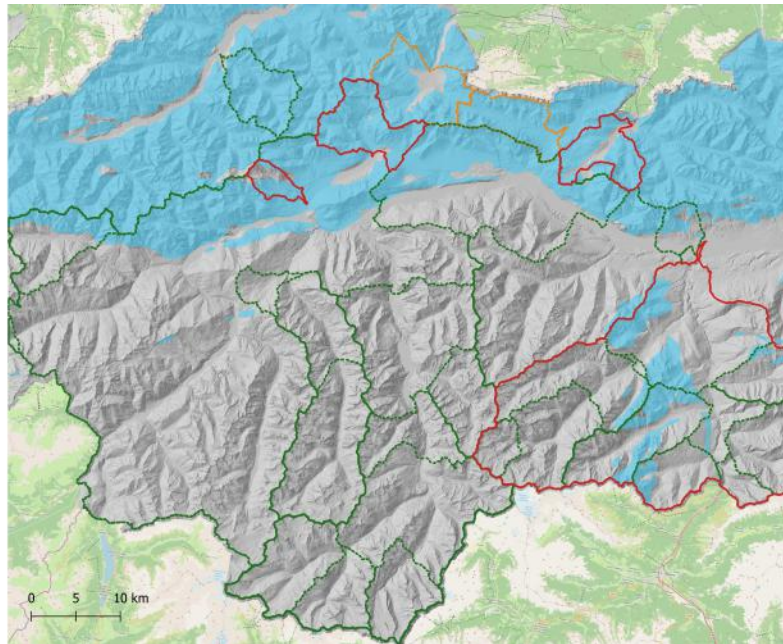


Figure 5.12: Map of all catchments. Those marked in red have no significant water level fluctuations. Marked in orange are catchments with 2 of the 4 years with no significant variation. The blue area indicates the distribution of limestone over the study area.

Karst formations often lead to very complex subsurface runoff, making it impractical to analyze the outlets solely based on surface water level fluctuations. Filtering out these catchments has led to an improvement in the Marin method, as shown in Figure 5.13.

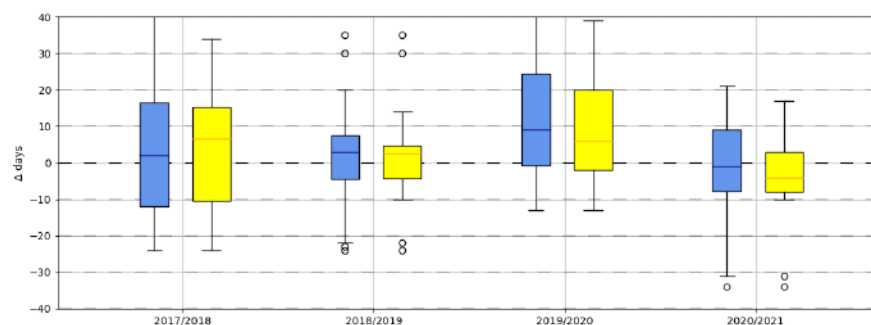


Figure 5.13: Schematic representation of the Marin method (blue) and the same method without the catchments showing no fluctuation (yellow) for each hydrological year separately compared to the melting detection of the water level data.

Excluding these catchments for the Beltramone method does not have any impact on the median value, as it remains unchanged. However,

the dispersion improves compared to the results when all catchments are included as shown in Figure A.15.

Chapter 6

Discussion

6.1 Response Time

As mentioned in Chapter 4.7, the average response time during the summer season is approximately one day for all catchments, regardless of their respective sizes. In the winter months, the runoff process can slow down, particularly in areas with high snow depths and saturated surface layers within the catchment.

6.2 Runoff Detection in a High Alpine Catchment

Normally, the initial signs of wetting are expected to be observed by the ascending pass (afternoon pass), but this is not the case for Figure 5.2. This is due to short melting processes that occur during some years. In these cases the repetition frequency of S1 is not sufficient to sample this situation. This leads to a moistening phase captured by the morning acquisition (descending pass) before the afternoon acquisition (Marin et al. 2020). The backscatter during the summer season exhibits a notable decrease in comparison to the winter season. This phenomenon can be attributed to the influence of soil moisture on the backscatter during the summer months, as the soil moisture has a high influence on the dielectric properties. Further, more than 55% of the catchment is covered by glacier, so at days with high radiation and high temperature the backscatter may contribute to melt water of the glacier ice.

6.3 Water level investigation

The Beltramone method and the Marin method are being evaluated using the water level data, assuming that the water level data are accurate and do not contain significant errors. It must be considered that solely water level data and no flow rates are available as ground truth data. A normalization was carried out followed by the application of a threshold for the gradient, to figure out the water increase due to melt. However this gradient threshold

might lead to different results for narrow stream beds compared to wide ones. The normalisation of water level data leads to apparently large fluctuations in very smooth time series, as even small events have a significant impact. This is particularly important for wide river channels, where even small increases in water level contribute significantly to the total volume of water. On the other hand, it might also falsify the result for narrow stream beds with low fluctuations, by indicating a false rise. The significant impact of these minimal variations on the identification of the discharge of melt water can often result in potentially inaccurate detection.

Furthermore, it is crucial to highlight that there are two significant water supply dams within the study area: the Gepatschspeicher and the Speichersee Finstertal. They serve as hydropower generation for Kaunertal and Kühtai, influencing the water level fluctuation highly. Moreover, the pumped-storage hydropower plant Kühtai has artificial supply pipes originating from the head of the Ötztal, Stubaital, and Oberbergthal valleys. This means that all 3 catchments have less drainage due to the artificial constructions. The same counts for the Kaunertal power plant, having artificial supply pipes from the Pitztal and the head of the Inntal valley. On the east and west side of the Kaunertal.

6.4 Snow retrieval with Sentinel-1 backscatter data

The ability to map snow with radar backscatter data from Sentinel 1 possesses certain limitations. One of the key factors to consider is the incidence angle, which significantly influences the backscatter.

The disparity between ascending and descending returns may arise due to varying acquisition geometries, illumination areas, and illumination times during data collection. The ascending mode refers to images acquired at 5 pm UTC, the descending mode refers to times at 5 am UTC. Moreover, the layover and shadowing mask affect different areas for ascending and descending pass. The ascending pass is partly blind to west facing slopes. Compared with the acquisition time of 5 pm UTC, it predominantly captures snow pixels associated with east-facing slopes in the evening after sunset. The snow covering the slopes that face east may have already formed a hard crust on its upper layer after the sun has set. This could potentially explain why the moistening phase is initially observed by the descending pass. At times, the backscatter signal exhibits distinct behavior during ascending and descending passes for a specific duration. This can be attributed to variations in acquisition time and alterations in the snow structure that occur within a single day. In the morning, the snow might be frozen and in the evening already wet. Even slight changes within the snow structure can have an enormous effect on the backscatter signal.

It should be considered that the VV and VH polarizations acquired by S1 usually provide coherent information, indicating a high level of correlation

between them. In some cases although, an inverse correlation of the signal appear during the ripening phase. The continuous diurnal melting and refreezing cycles might generate ice layers, affecting the VV and VH polarization in different ways (Dozier et al. 1999).

Moreover, the repetition frequency of the S1 overflights is about 6 days for each relative orbit, resulting in gaps of several days between newly recorded scenes. Consequently, this hinders the ability to accurately capture the exact runoff day compared to the water level data.

The median for the winter of 2019/2020 showed significantly higher results than the other three years, most likely due to the low snow depth. It is important to note that snow depth is only measured at three specific in-situ stations, and therefore, these pointwise measurements should be distinguished from area-wide coverage. However, the low snow depth did result in pixels that were not fully covered by snow, making it challenging to detect snowmelt for the surrounding pixels. It is worth noting that these snow-free pixels were not masked out and still contributed to the observed result.

A technique was tested that took into account the cross-correlation between the water data and the backscatter data. Consequently, the water level data was carefully examined to identify and exclude any instances of rain events, ensuring their influence was eliminated. However this did not give any reasonable results, as the gradient of both datasets are rather dissimilar and therefore not mentioned in the results chapter.

6.5 Enhancing Beltramone Method

As the Beltramone method did not deliver satisfying results, some enhancements of the method were tested. An idea was to capture the anomaly-date not only for the descending VV timeline but for each of the four timelines separately. Constructing the mean over multiple days aimed to establish a more robust approach with increased input data. However, this approach proved to be unsuccessful as the outcomes appeared to be arbitrary. Even when considering individual time series, there was no enhancement observed in the results.

Chapter 7

Conclusion & Outlook

In this work, the relationship between snowmelt dynamics from backscatter data and the water level rise from water gauge is investigated. For this purpose the the catchment boundaries of the water outlets are introduced. The backscattering snowmelt is based on the methods by Beltramone et al. (2023) and Marin et al. (2020). The implementation of the Marin method involved dividing the backscatter time series into distinct phases of snowmelt dynamics, namely moistening, ripening, and runoff. Subsequently, the time delay of the runoff phase was compared to the increase in water level. The Beltramone method utilizes derivatives of the backscatter time series to examine anomalies and estimate the runoff date. The results showed clearly that the Marin method is more robust and accurate than the Beltramone approach.

Splitting the catchments into aspect related slopes might improve the findings as snow conditions differ strongly with respect to the incoming radiation. Furthermore, a elevation threshold implemented for all catchments could help to clarify the behaviour of the timeline. This elevation threshold could be introduced in 50-100 m steps, so the snowmelt dynamics within the season and elevation dependent can be analysed. It would also be interesting to see how slope steepness contributes to runoff time. Moreover, the geology plays an important role with respect to the runoff pattern. Going deeper into geology investigation might help to further improve the findings.

Bibliography

- Abe, Takahiro, Go Iwahana, Petr Efremov, Alexey Desyatkin, Takumi Kawamura, Alexander Fedorov, Yuri Zhegusov, Kazuki Yanagiya, and Takeo Tadono (Sept. 2020). “Surface displacement revealed by L-band InSAR analysis in the Mayya area, Central Yakutia, underlain by continuous permafrost”. In: *Earth, Planets and Space* 72, p. 138. DOI: 10.1186/s40623-020-01266-3.
- Alonso, Rafael, José Pozo, Samuel Buisan, and Adolfo Alvarez (Feb. 2021). “Analysis of the Snow Water Equivalent at the AEMet-Formigal Field Laboratory (Spanish Pyrenees) During the 2019/2020 Winter Season Using a Stepped-Frequency Continuous Wave Radar (SFCW)”. In: *Remote Sensing* 13, p. 616. DOI: 10.3390/rs13040616.
- American Avalanche Association, US Forest Service National Avalanche Center (2023). *Avalanche Encyclopedia*. <https://avalanche.org/avalanche-encyclopedia/snowpack/weak-layer/>. Accessed: 2023-06-29. (Visited on 06/29/2023).
- Baggi, Stefano and Juerg Schweizer (July 2008). “Characteristics of wet-snow avalanche activity: 20 years of observations from a high alpine valley (Dischma, Switzerland)”. In: *Natural Hazards* 50, pp. 97–108. DOI: 10.1007/s11069-008-9322-7.
- Barnhart, Theodore B., Christina L. Tague, and Noah P. Molotch (2020). “The Counteracting Effects of Snowmelt Rate and Timing on Runoff”. In: *Water Resources Research* 56.8. e2019WR026634. DOI: <https://doi.org/10.1029/2019WR026634>. eprint: <https://agupubs.onlinelibrary.wiley.com/doi/pdf/10.1029/2019WR026634>. URL: <https://agupubs.onlinelibrary.wiley.com/doi/abs/10.1029/2019WR026634>.
- Bauer-Marschallinger, Bernhard (2015). *The Equi7 Grid*. https://cartography.tuwien.ac.at/eurocarto/wp-content/uploads/2015/09/3_6_ppt.pdf. Accessed: 2023-11-08. (Visited on 11/10/2015).
- Bauer-Marschallinger, Bernhard, Daniel Sabel, and Wolfgang Wagner (2014). “Optimisation of global grids for high-resolution remote sensing data”. In: *Computers & Geosciences* 72, pp. 84–93. ISSN: 0098-3004. DOI: <https://doi.org/10.1016/j.cageo.2014.07.005>. URL: <https://www.sciencedirect.com/science/article/pii/S0098300414001629>.
- Becker, Alfred (2005). “Runoff Processes in Mountain Headwater Catchments: Recent Understanding and Research Challenges”. In: *Global*

- Change and Mountain Regions: An Overview of Current Knowledge*. Ed. by Uli M. Huber, Harald K. M. Bugmann, and Mel A. Reasoner. Dordrecht: Springer Netherlands, pp. 283–295. DOI: 10.1007/1-4020-3508-X_29. URL: https://doi.org/10.1007/1-4020-3508-X_29.
- Beltramone, Giuliana, Alejandro C. Frery, Camilo H. Rotela, Alba Germán, Matías Bonansea, C. Marcelo Scavuzzo, and Anabella Ferral (2023). “Identification of Seasonal Snow Phase Changes From C-Band SAR Time Series With Dynamic Thresholds”. In: *IEEE Journal of Selected Topics in Applied Earth Observations and Remote Sensing* 16, pp. 6995–7008. DOI: 10.1109/JSTARS.2023.3281149.
- Blankinship, Joseph C., Matthew W. Meadows, Ryan G. Lucas, and Stephen C. Hart (2014). “Snowmelt timing alters shallow but not deep soil moisture in the Sierra Nevada”. In: *Water Resources Research* 50.2, pp. 1448–1456. DOI: <https://doi.org/10.1002/2013WR014541>. eprint: <https://agupubs.onlinelibrary.wiley.com/doi/pdf/10.1002/2013WR014541>. URL: <https://agupubs.onlinelibrary.wiley.com/doi/abs/10.1002/2013WR014541>.
- Buchelt, S., K. Skov, K. K. Rasmussen, and T. Ullmann (2022). “Sentinel-1 time series for mapping snow cover depletion and timing of snowmelt in Arctic periglacial environments: case study from Zackenberg and Kobbefjord, Greenland”. In: *The Cryosphere* 16.2, pp. 625–646. DOI: 10.5194/tc-16-625-2022. URL: <https://tc.copernicus.org/articles/16/625/2022/>.
- Dietz, Andreas, Claudia Kuenzer, Ursula Gessner, and Stefan Dech (July 2012). “Remote Sensing of Snow – a Review of available methods.” In: *International Journal of Remote Sensing* 33, pp. 4094–4134. DOI: 10.1080/01431161.2011.640964.
- Dingman, S. L. (2015). *Physical hydrology* /. Third edition. Long Grove, Illinois : Waveland Press, Inc.,
- Dozier, Jeff and Rick Kattelmann (Jan. 1999). “Observations of snowpack ripening in the Sierra Nevada, R. Kattelmann and J. Dozier, 1999, Journal of Glaciology”. In: *Journal of Glaciology* 45, pp. 409–416.
- ESA (2023). *Sentinel-1 User Guides*. <https://sentinels.copernicus.eu/web/sentinel/user-guides/sentinel-1-sar>. Accessed: 2023-06-19. (Visited on 06/19/2023).
- GeoSphereAustria (2023). *Stationsdaten Data Hub*. <https://data.hub.geosphere.at/group/stationsdaten>. Accessed: 2023-12-19. (Visited on 12/19/2023).
- Grimaldi, Salvatore, Fernando Nardi, Francesco Di Benedetto, Erkan Istanbulluoglu, and Rafael L. Bras (2007). “A physically-based method for removing pits in digital elevation models”. In: *Advances in Water Resources* 30.10. Recent Developments in Hydrologic Analysis, pp. 2151–2158. ISSN: 0309-1708. DOI: <https://doi.org/10.1016/j.advwatres.2006.11.016>. URL: <https://www.sciencedirect.com/science/article/pii/S0309170807000644>.
- Gunn, Grant E., Marco Brogioni, Claude Duguay, Giovanni Macelloni, Andrew Kasurak, and Joshua King (2015). “Observation and Modeling of X- and Ku-Band Backscatter of Snow-Covered Freshwater Lake Ice”.

- In: *IEEE Journal of Selected Topics in Applied Earth Observations and Remote Sensing* 8.7, pp. 3629–3642. DOI: 10.1109/JSTARS.2015.2420411.
- Hamdan, Omar, Hamzah Khali Aziz, and Mohd Hasmadi (2014). “L-band ALOS PALSAR for biomass estimation of Matang Mangroves, Malaysia”. In: *Remote Sensing of Environment* 155, pp. 69–78. ISSN: 0034-4257. DOI: <https://doi.org/10.1016/j.rse.2014.04.029>. URL: <https://www.sciencedirect.com/science/article/pii/S0034425714001898>.
- Hiebl, Johann and Christoph Frei (Feb. 2015). “Daily temperature grids for Austria since 1961—concept, creation and applicability”. In: *Theoretical and Applied Climatology* 124. DOI: 10.1007/s00704-015-1411-4.
- (Mar. 2017). “Daily precipitation grids for Austria since 1961—development and evaluation of a spatial dataset for hydroclimatic monitoring and modelling”. In: *Theoretical and Applied Climatology* 132. DOI: 10.1007/s00704-017-2093-x.
- Hydro Online* (2023). <https://wiski.tirol.gv.at/hydro/#/Wasserstand?station=201525>. Accessed: 2023-11-02. (Visited on 11/02/2023).
- Irwin, Katherine, Alexander Braun, Georgia Fotopoulos, Achim Roth, and Birgit Wessel (2018). “Assessing Single-Polarization and Dual-Polarization TerraSAR-X Data for Surface Water Monitoring”. In: *Remote Sensing* 10.6. ISSN: 2072-4292. DOI: 10.3390/rs10060949. URL: <https://www.mdpi.com/2072-4292/10/6/949>.
- Juras, Roman, Johanna Blöcher, Michal Jenicek, Ondrej Hotovy, and Yannis Markonis (2021). “What affects the hydrological response of rain-on-snow events in low-altitude mountain ranges in Central Europe?” In: *Journal of Hydrology* 603, p. 127002. ISSN: 0022-1694. DOI: <https://doi.org/10.1016/j.jhydrol.2021.127002>. URL: <https://www.sciencedirect.com/science/article/pii/S0022169421010520>.
- Karbou, Fatima, Guillaume James, Philippe Durand, and A.M. Atto (Dec. 2021). “Thresholds and Distances to Better Detect Wet Snow over Mountains with Sentinel-1 Image Time Series”. In: pp. 127–144. ISBN: 9781789450569. DOI: 10.1002/9781119882268.ch5.
- Karbou, Fatima, Gaëlle Veyssière, Cécile Coleou, Anne Dufour, Isabelle Gouttevin, Philippe Durand, Simon Gascoin, and Manuel Grizonnet (2021). “Monitoring Wet Snow Over an Alpine Region Using Sentinel-1 Observations”. In: *Remote Sensing* 13.3. ISSN: 2072-4292. DOI: 10.3390/rs13030381. URL: <https://www.mdpi.com/2072-4292/13/3/381>.
- Kirimi, Fridah, David N. Kuria, Frank Thonfeld, Esther Amler, Kenneth Mubea, Salome Misana, and Gunter Menz (2016). “Influence of Vegetation Cover on the Oh Soil Moisture Retrieval Model: A Case Study of the Malinda Wetland, Tanzania”. In: *ARS* 5, pp. 28–42. URL: <https://api.semanticscholar.org/CorpusID:3759307>.
- Kobayashi, Daiji and Hideaki Motoyama (Jan. 1985). “Effect of Snow Cover on Time Lag of Runoff from a Watershed”. In: *Annals of Glaciology* 6. DOI: 10.1017/S0260305500010144.
- Koch, Franziska, Patrick Henkel, Florian Appel, Lino Schmid, Heike Bach, Markus Lamm, Monika Prasch, Jürg Schweizer, and Wolfram Mauser (2019). “Retrieval of Snow Water Equivalent, Liquid Water Content,

- and Snow Height of Dry and Wet Snow by Combining GPS Signal Attenuation and Time Delay”. In: *Water Resources Research* 55.5, pp. 4465–4487. DOI: <https://doi.org/10.1029/2018WR024431>. URL: <https://agupubs.onlinelibrary.wiley.com/doi/abs/10.1029/2018WR024431>.
- Lastrada, Eduardo, Guillermo Cobos, Julio Garzón-Roca, and F. Javier Torrijo (2021). “Seasonal Variability of Snow Density in the Spanish Pyrenees”. In: *Water* 13.11. ISSN: 2073-4441. DOI: 10.3390/w13111598. URL: <https://www.mdpi.com/2073-4441/13/11/1598>.
- Lauknes, Tom Rune (2004). “Long-Term Surface Deformation Mapping using Small-Baseline Differential SAR Interferograms”. In: URL: <https://api.semanticscholar.org/CorpusID:12348152>.
- Lievens, Hans et al. (Oct. 2019). “Snow depth variability in the Northern Hemisphere mountains observed from space”. In: *Nature Communications* 10, pp. 1–12. DOI: 10.1038/s41467-019-12566-y.
- Lindsay, John (Sept. 2015). “Efficient hybrid breaching-filling sink removal methods for flow path enforcement in digital elevation models”. In: *Hydrological Processes* 30, pp. 846–857. DOI: 10.1002/hyp.10648.
- Liu, Qingquan, Qing Ji, Xiaoping Pang, Xin Gao, Xi Zhao, and Ruibo Lei (2018). “Inter-Calibration of Passive Microwave Satellite Brightness Temperatures Observed by F13 SSM/I and F17 SSMIS for the Retrieval of Snow Depth on Arctic First-Year Sea Ice”. In: *Remote Sensing* 10.1. ISSN: 2072-4292. DOI: 10.3390/rs10010036. URL: <https://www.mdpi.com/2072-4292/10/1/36>.
- Marin, C., G. Bertoldi, V. Premier, M. Callegari, C. Brida, K. Hürkamp, J. Tschiersch, M. Zebisch, and C. Notarnicola (2020). “Use of Sentinel-1 radar observations to evaluate snowmelt dynamics in alpine regions”. In: *The Cryosphere* 14.3, pp. 935–956. DOI: 10.5194/tc-14-935-2020. URL: <https://tc.copernicus.org/articles/14/935/2020/>.
- Merz, Ralf and Günter Blöschl (Dec. 2003). “A process typology of regional floods”. In: *Water Resources Research - WATER RESOUR RES* 39. DOI: 10.1029/2002WR001952.
- Moreira, Alberto, Pau Prats-Iraola, Marwan Younis, Gerhard Krieger, Irena Hajnsek, and Konstantinos P. Papathanassiou (2013). “A tutorial on synthetic aperture radar”. In: *IEEE Geoscience and Remote Sensing Magazine* 1.1, pp. 6–43. DOI: 10.1109/MGRS.2013.2248301.
- Mouche, Alexis, Bertrand Chapron, Biao Zhang, and Romain Husson (July 2017). “Combined Co- and Cross-Polarized SAR Measurements Under Extreme Wind Conditions”. In: *IEEE Transactions on Geoscience and Remote Sensing* 99. DOI: 10.1109/TGRS.2017.2732508.
- Naderpour, Reza and Mike Schwank (2018). “Snow Wetness Retrieved from L-Band Radiometry”. In: *Remote Sensing* 10.3. ISSN: 2072-4292. DOI: 10.3390/rs10030359. URL: <https://www.mdpi.com/2072-4292/10/3/359>.
- Nagler, Thomas and Helmut Rott (2000). “Retrieval of wet snow by means of multitemporal SAR data”. In: *IEEE Transactions on Geoscience and Remote Sensing* 38 (2 I), pp. 754–765. ISSN: 01962892. DOI: 10.1109/36.842004.

- Nagler, Thomas, Helmut Rott, Elisabeth Ripper, Gabriele Bippus, and Markus Hetzenecker (2016). “Advancements for Snowmelt Monitoring by Means of Sentinel-1 SAR”. In: *Remote Sensing* 8.4. ISSN: 2072-4292. DOI: 10.3390/rs8040348. URL: <https://www.mdpi.com/2072-4292/8/4/348>.
- NASA (2023). *What is Synthetic Aperture System?* <https://www.earthdata.nasa.gov/learn/backgrounders/what-is-sar>. Accessed: 2023-10-12. (Visited on 10/12/2023).
- Navacchi Claudio and Raml, Bernhard, Sebastian Hahn, Bernhard Bauer-Marschallinger, and Nikolaus Dräger (2022). *yeoda*. <https://github.com/TUW-GEO/yeoda>. Accessed: 2022-11-15. DOI: <https://doi.org/10.5281/zenodo.5593090>. (Visited on 11/15/2022).
- Nave, R. (2023). *Classification of Polarization*. <http://hyperphysics.phy-astr.gsu.edu/hbase/phyopt/polclas.html>. Accessed: 2023-10-17. (Visited on 10/17/2023).
- O’Callaghan, John F. and David M. Mark (1984). “The extraction of drainage networks from digital elevation data”. In: *Computer Vision, Graphics, and Image Processing* 28.3, pp. 323–344. ISSN: 0734-189X. DOI: [https://doi.org/10.1016/S0734-189X\(84\)80011-0](https://doi.org/10.1016/S0734-189X(84)80011-0). URL: <https://www.sciencedirect.com/science/article/pii/S0734189X84800110>.
- OEAV (2023). *Spannungsfeld Energiepolitik und Gewässerschutz*. https://www.alpenverein.at/portal/natur-umwelt/alpine_raumordnung/wasserkraft/index.php. (Visited on 10/18/2023).
- Oki, Taikan, Dara Entekhabi, and T. Harrold (Jan. 2004). “The global water cycle”. In: *Washington DC American Geophysical Union Geophysical Monograph Series*, pp. 225–237. DOI: 10.1029/150GM18.
- Patil, Akshay, Gulab Singh, and Christoph Rüdiger (2020). “Retrieval of Snow Depth and Snow Water Equivalent Using Dual Polarization SAR Data”. In: *Remote Sensing* 12.7. ISSN: 2072-4292. DOI: 10.3390/rs12071183. URL: <https://www.mdpi.com/2072-4292/12/7/1183>.
- Pivot, Frédérique C. (2012). “C-Band SAR Imagery for Snow-Cover Monitoring at Treeline, Churchill, Manitoba, Canada”. In: *Remote Sensing* 4.7, pp. 2133–2155. ISSN: 2072-4292. DOI: 10.3390/rs4072133. URL: <https://www.mdpi.com/2072-4292/4/7/2133>.
- Qin, Cheng-Zhi and Lijun Zhan (2012). “Parallelizing flow-accumulation calculations on graphics processing units—From iterative DEM preprocessing algorithm to recursive multiple-flow-direction algorithm”. In: *Computers & Geosciences* 43, pp. 7–16. ISSN: 0098-3004. DOI: <https://doi.org/10.1016/j.cageo.2012.02.022>. URL: <https://www.sciencedirect.com/science/article/pii/S0098300412000787>.
- Raney, R.K., H. Runge, R. Bamler, I.G. Cumming, and F.H. Wong (1994). “Precision SAR processing using chirp scaling”. In: *IEEE Transactions on Geoscience and Remote Sensing* 32.4, pp. 786–799. DOI: 10.1109/36.298008.
- Ribis, Markus (2013). “The Rock Glacier Inventory of Tyrol - A contribution to permafrost research”. In.
- Rott, Helmut, Don Cline, Claude Duguay, Richard Essery, Christian Haas, Giovanni Macelloni, Eirik Malnes, Jouni Pulliainen, Helge Rebhan, and

- Simon Yueh (2008). “CoReH2O - A Ku- and X-Band SAR Mission for Snow and Ice Monitoring”. In: *7th European Conference on Synthetic Aperture Radar*, pp. 1–4.
- Schanda, Erwin (1986). *Physical Fundamentals of Remote Sensing*. URL: <https://api.semanticscholar.org/CorpusID:117973590>.
- Schepaschenko, Dmitry et al. (2015). “Development of a global hybrid forest mask through the synergy of remote sensing, crowdsourcing and FAO statistics”. In: *Remote Sensing of Environment* 162, pp. 208–220. ISSN: 0034-4257. DOI: <https://doi.org/10.1016/j.rse.2015.02.011>. URL: <https://www.sciencedirect.com/science/article/pii/S0034425715000644>.
- Schubert, Gerhard, Rudolf Berka, Christian Katzlberger, Klaus Motschka, Monika Denner, Johannes Grath, and Rudolf Philippitsch (2018). “Radionuclides in groundwater, rocks and stream sediments in Austria – results from a recent survey”. In: *Geological Society, London, Special Publications* 451.1, pp. 83–112. DOI: 10.1144/SP451.10. eprint: <https://www.lyellcollection.org/doi/pdf/10.1144/SP451.10>. URL: <https://www.lyellcollection.org/doi/abs/10.1144/SP451.10>.
- Schwank, Mike and Reza Naderpour (2018). “Snow Density and Ground Permittivity Retrieved from L-Band Radiometry: Melting Effects”. In: *Remote Sensing* 10.2. ISSN: 2072-4292. DOI: 10.3390/rs10020354. URL: <https://www.mdpi.com/2072-4292/10/2/354>.
- Shi, Jiancheng and J. Dozier (1995). “Inferring snow wetness using C-band data from SIR-C’s polarimetric synthetic aperture radar”. In: *IEEE Transactions on Geoscience and Remote Sensing* 33.4, pp. 905–914. DOI: 10.1109/36.406676.
- Small, David (2011). “Flattening Gamma: Radiometric Terrain Correction for SAR Imagery”. In: *IEEE Transactions on Geoscience and Remote Sensing* 49.8, pp. 3081–3093. DOI: 10.1109/TGRS.2011.2120616.
- Sommerfeld, R. A. and E. LaChapelle (1970a). “The Classification of Snow Metamorphism”. In: *Journal of Glaciology* 9.55, pp. 3–18. DOI: 10.3189/S0022143000026757.
- (1970b). “The Classification of Snow Metamorphism”. In: *Journal of Glaciology* 9.55, pp. 3–18. DOI: 10.3189/S0022143000026757.
- Taheri, Mercedeh and Abdolmajid Mohammadian (2022). “An Overview of Snow Water Equivalent: Methods, Challenges, and Future Outlook”. In: *Sustainability* 14.18. ISSN: 2071-1050. DOI: 10.3390/su141811395. URL: <https://www.mdpi.com/2071-1050/14/18/11395>.
- Tsai, Ya-Lun S., Andreas Dietz, Natascha Oppelt, and Claudia Kuenzer (2019). “Remote Sensing of Snow Cover Using Spaceborne SAR: A Review”. In: *Remote Sensing* 11.12. ISSN: 2072-4292. DOI: 10.3390/rs11121456. URL: <https://www.mdpi.com/2072-4292/11/12/1456>.
- Tsokas, Arsenios, Maciej Rysz, Panos M. Pardalos, and Kathleen Dipple (2022). “SAR data applications in earth observation: An overview”. In: *Expert Systems with Applications* 205, p. 117342. ISSN: 0957-4174. DOI: <https://doi.org/10.1016/j.eswa.2022.117342>. URL: <https://www.sciencedirect.com/science/article/pii/S0957417422006960>.

- Ulaby, Fawwaz, David Long, William Blackwell, Charles Elachi, Adrian Fung, Christopher Ruf, K. Sarabandi, Jakob Zyl, and Howard Zebker (Jan. 2014). *Microwave Radar and Radiometric Remote Sensing*, p. 984. ISBN: 978-0-472-11935-6.
- Viviroli, Daniel, Hans H. Dürr, Bruno Messerli, Michel Meybeck, and Rolf Weingartner (2007). “Mountains of the world, water towers for humanity: Typology, mapping, and global significance”. In: *Water Resources Research* 43.7. DOI: <https://doi.org/10.1029/2006WR005653>. eprint: <https://agupubs.onlinelibrary.wiley.com/doi/pdf/10.1029/2006WR005653>. URL: <https://agupubs.onlinelibrary.wiley.com/doi/abs/10.1029/2006WR005653>.
- Wagner, Beatrice, Christoph Hauer, Angelika Schoder, and Helmut Habersack (2015). “A review of hydropower in Austria: Past, present and future development”. In: *Renewable and Sustainable Energy Reviews* 50, pp. 304–314. ISSN: 1364-0321. DOI: <https://doi.org/10.1016/j.rser.2015.04.169>. URL: <https://www.sciencedirect.com/science/article/pii/S1364032115004396>.
- Wagner, Thomas, Alexander Brodacz, Karl Krainer, and Gerfried Winkler (June 2020). “Active rock glaciers as shallow groundwater reservoirs, Austrian Alps (Aktive Blockgletscher als seichte Grundwasserspeicher der österreichischen Alpen)”. In: *Grundwasser*. DOI: 10.1007/s00767-020-00455-x.
- Wang, Yunlong, Xiaodong Huang, Hui Liang, Yanhua Sun, Qisheng Feng, and Tiangang Liang (2018). “Tracking Snow Variations in the Northern Hemisphere Using Multi-Source Remote Sensing Data (2000–2015)”. In: *Remote Sensing* 10.1. ISSN: 2072-4292. DOI: 10.3390/rs10010136. URL: <https://www.mdpi.com/2072-4292/10/1/136>.
- Winkler, Gerfried, Thomas Wagner, Marcus Pauritsch, Steffen Birk, Andreas Kellerer-Pirklbauer, Ralf Benischke, Albrecht Leis, Rainer Morawetz, Marcellus G. Schreilechner, and Stefan Hergarten (2016). “Identification and assessment of groundwater flow and storage components of the relict Schöneben Rock Glacier, Niedere Tauern Range, Eastern Alps (Austria)”. English. In: *Hydrogeology Journal* 24, pp. 937–953. ISSN: 1431-2174. DOI: 10.1007/s10040-015-1348-9.
- WMO (2023a). *Essential Climate Variables*. <https://public.wmo.int/en/programmes/global-climate-observing-system/essential-climate-variables>. Accessed: 2023-11-07. (Visited on 11/07/2023).
- (2023b). *Essential Climate Variables*. <https://public.wmo.int/en/programmes/global-climate-observing-system/essential-climate-variables>. Accessed: 2023-10-17. (Visited on 10/17/2023).
- Würzer, Sebastian, Tobias Jonas, Nander Wever, and Michael Lehning (2016). “Influence of Initial Snowpack Properties on Runoff Formation during Rain-on-Snow Events”. In: *Journal of Hydrometeorology* 17.6, pp. 1801–1815. DOI: <https://doi.org/10.1175/JHM-D-15-0181.1>. URL: https://journals.ametsoc.org/view/journals/hydr/17/6/jhm-d-15-0181_1.xml.

BIBLIOGRAPHY

Zanaga, Daniele et al. (Oct. 2021). *ESA WorldCover 10 m 2020 v100*.
Version v100. DOI: 10.5281/zenodo.5571936. URL: <https://doi.org/10.5281/zenodo.5571936>.

Appendix

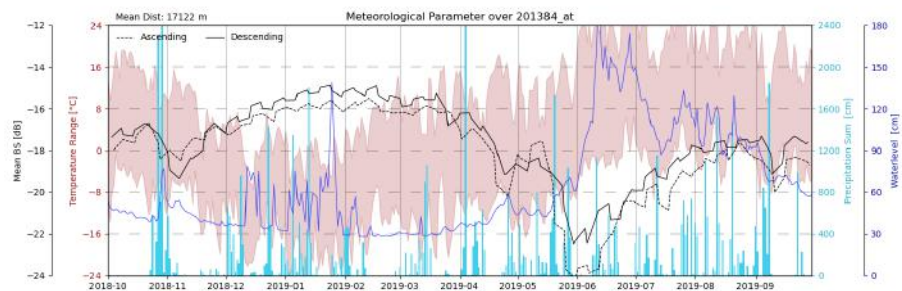


Figure A.1: Meteorological comparison of the VH backscatter data for catchment 201384 shows a very cold period between the beginning of December until the start of February for the hydrological year 2018/20219.

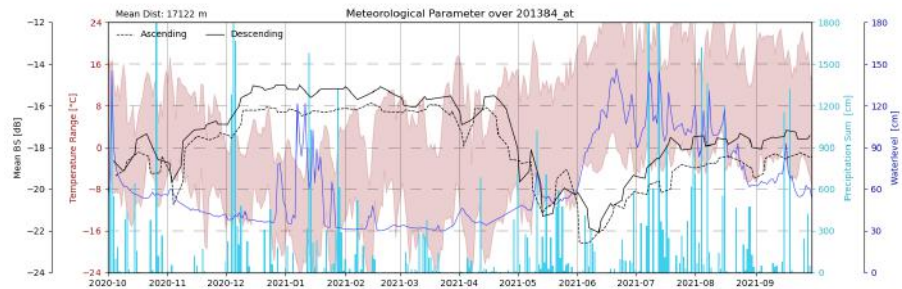


Figure A.2: Meteorological comparison of the VV backscatter data for catchment 201384 shows very cold days in December and at the beginning on January for the hydrological year 2020/2021.

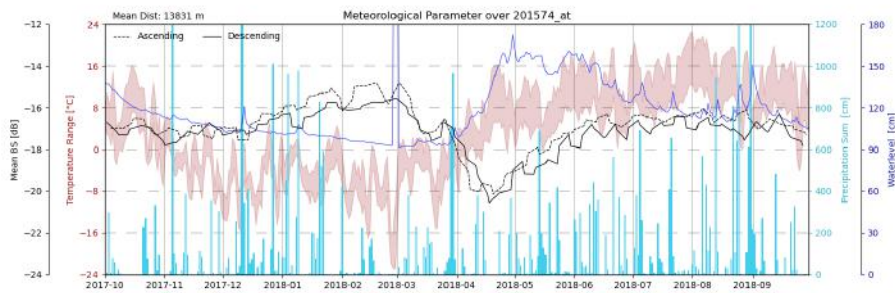


Figure A.3: Meteorological comparison of the VV backscatter data for catchment 201574 shows very cold days in February for the hydrological year 2017/2018.

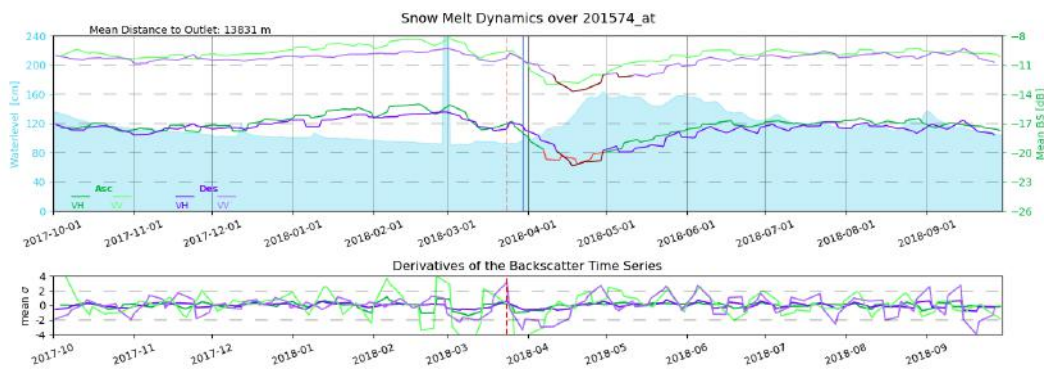


Figure A.4: Backscatter distribution for time series without 15 % forest cover shows only a slight drop of the signal in the wetting phase, therefore further investigation is needed.

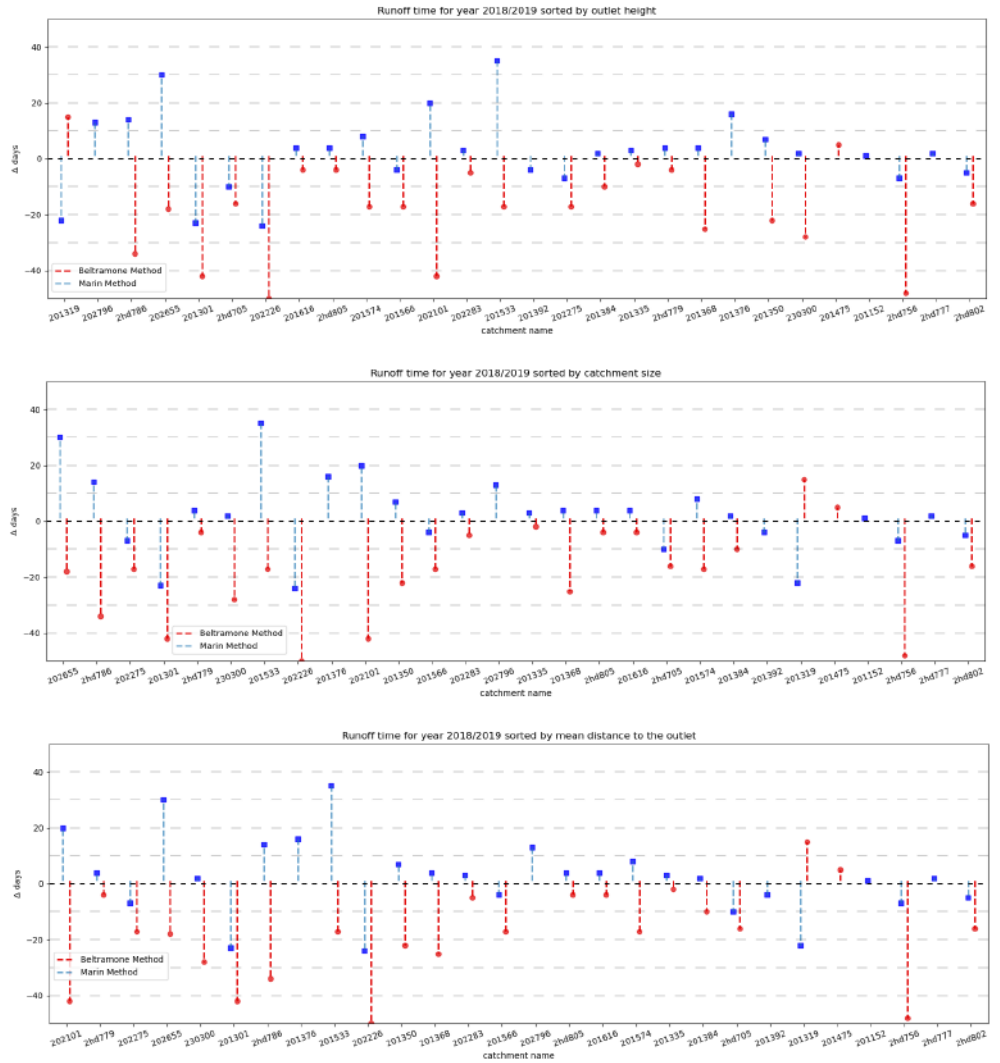


Figure A.5: The image provided shows the different catchments sorted by (1) outlet height, (2) catchment size and (3) mean distance to outlet. The values are sorted from minimal to maximal value, if the information is provided in the metadata. Information is not provided for the last 4 catchments.

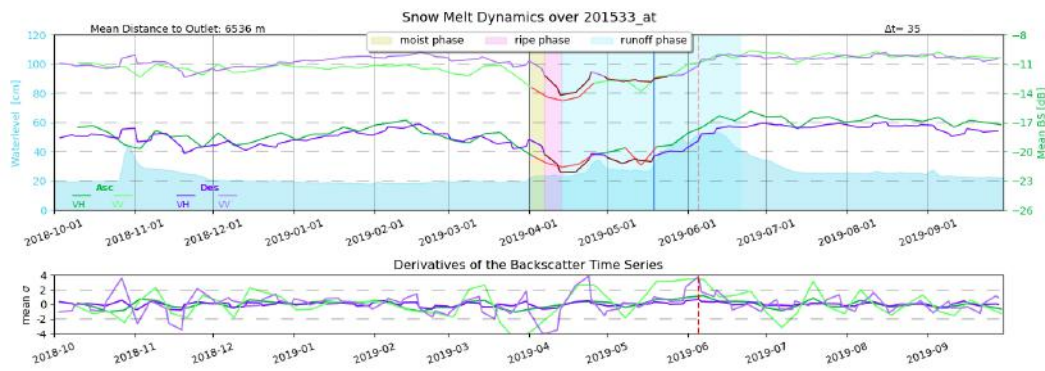


Figure A.6: Snowmelt dynamics for the catchment 201533 shows a very early beginning of the melting phases, whereas the increase in the water signal is detected a month later.

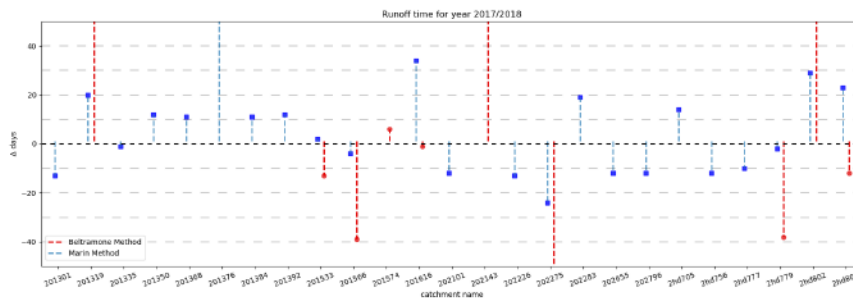


Figure A.7: Runoff time for each catchment for the hydrological year 2017/2018 showing the time difference between the Marin Method (blue) and the Beltramone Method (red).

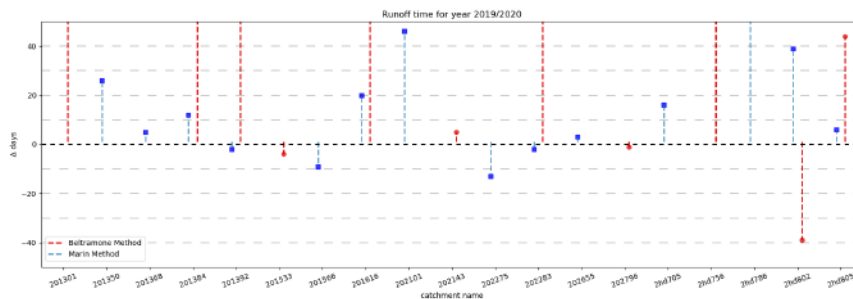


Figure A.8: Runoff time for each catchment for the hydrological year 2018/2019 showing the time difference between the Marin Method (blue) and the Beltramone Method (red).

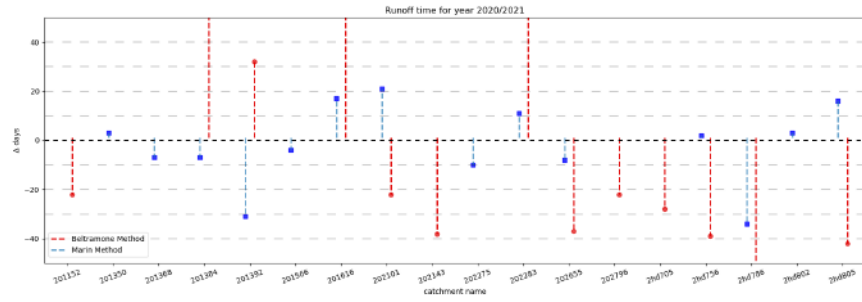


Figure A.9: Runoff time for each catchment for the hydrological year 2020/2021 showing the time difference between the Marin Method (blue) and the Beltramone Method (red).

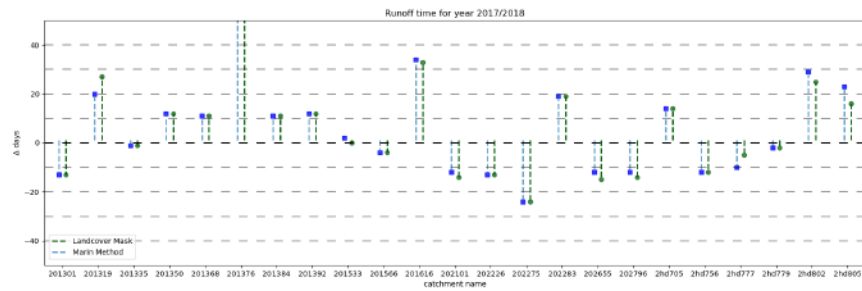


Figure A.10: Runoff time for each catchment for the hydrological year 2017/2018 showing the time difference between the Marin Method (blue) and the Method without Forest pixels (green).

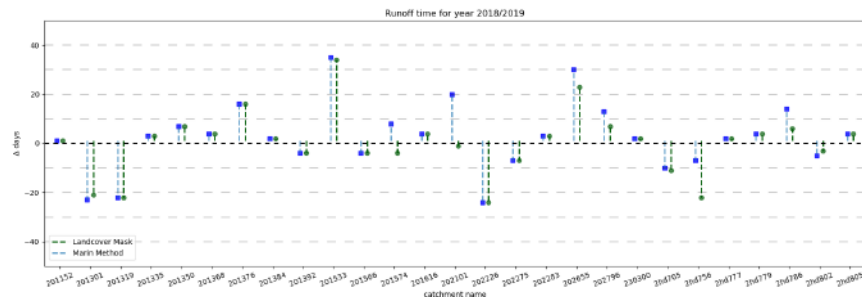


Figure A.11: Runoff time for each catchment for the hydrological year 2018/2019 showing the time difference between the Marin Method (blue) and the Method without Forest pixels (green).

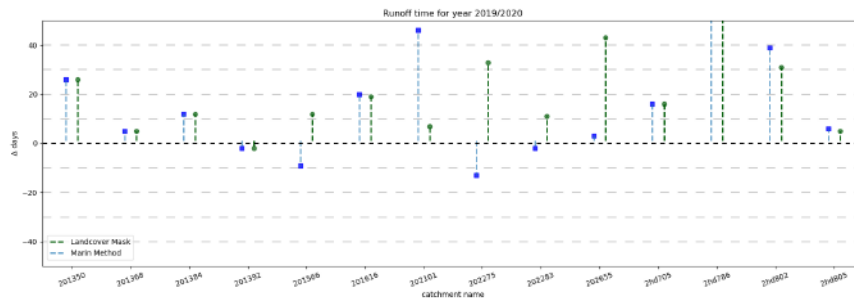


Figure A.12: Runoff time for each catchment for the hydrological year 2019/2020 showing the time difference between the Marin Method (blue) and the Method without Forest pixels (green).

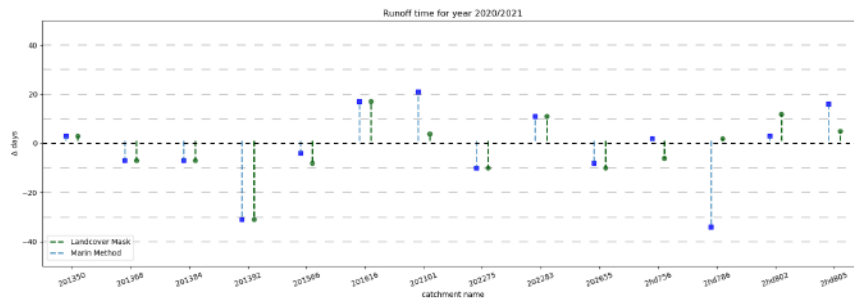


Figure A.13: Runoff time for each catchment for the hydrological year 2020/2021 showing the time difference between the Marin Method (blue) and the Method without Forest pixels (green).

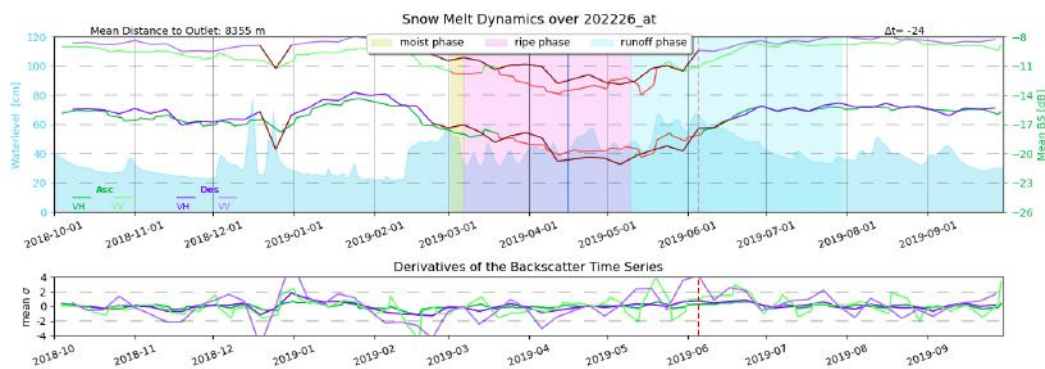


Figure A.14: This catchment at the very north west of the study area shows high fluctuating water level. The Backscatter shows a clear drop of signal. The melting start in the water level data is not clearly detectable.

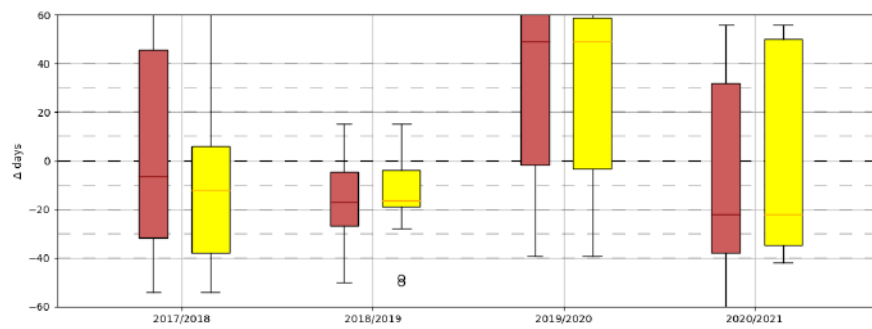


Figure A.15: Schematic representation of the Beltramone Results (red) and the same Method without the catchments with no fluctuation (yellow) for each hydrological year separately.